Strain localization and weakening induced by interplay between deformation and reaction: experimentally deformed plagioclase-pyroxene assemblages

Nicolas Mansard[1,*], Holger Stünitz[1,2], Hugues Raimbourg[1] and Jacques Précigout[1]

[1] Institut des Sciences de la Terre d'Orléans (ISTO), UMR 7327, CNRS/BRGM, Université d'Orléans, 45071 Orléans, France

[2] Department of Geology, University of Tromsø, Dramsveien 201, 9037 Tromsø, Norway

To be published in Journal of Structural Geology.

*Corresponding author at : UMR 7327, Institut des Sciences de la Terre d'Orléans (ISTO), Université d'Orléans, 1A rue de la Férollerie, 45071 Orléans, France. Telephone numbers : +33 6 59 49 73 42.

E-mail adresses : nicolas.mansard@cnrs-orleans.fr *(N. Mansard),* holger.stunitz@uit.no *(H. Stünitz),* hugues.raimbourg@univ-orleans.fr *(H. Raimbourg),* jacques.precigout@univ-orleans.fr *(J. Précigout).*

Keywords : Rock deformation experiments; Mineral reactions; Dissolution-precipitation creep; Strain localization.

Abstract

In order to study the mutual effect of deformation and mineral reactions, we have conducted shear experiments on fine-grained plagioclase-pyroxene assemblages in a Griggs-type solid-medium deformation apparatus. Experiments were performed at a constant shear strain rate of 10^{-5} s^{-1}, a confining pressure of 1 GPa and temperatures between 800 and 900 °C. Whereas the peak stress of plagioclase + pyroxene assemblages is documented between the ones of the end-member phases, the strength of polymineralic materials strongly weakens after peak stress and reaches flow stresses that stabilize far below those of the weaker phase (plagioclase). This weakening correlates with the coeval development of high-strain shear zones where new phases are preferentially produced, including new pyroxene, plagioclase and amphibole with different compositions with respect to the starting material. The reaction product mostly occurs as intimately mixed phases within interconnected and fine-grained shear bands. Altogether, these features demonstrate that deformation significantly enhances the kinetics of mineral reactions, which in turn strongly weaken the deforming sample through strain localization and phase nucleation, both probably driven by grain-size-sensitive pressure-solution creep. Such an interplay between deformation and mineral reactions may have strong implications for the development and durability of crustal shear zones.

1. Introduction

Strain localization and resulting shear zones are considered to be fundamental features of plate tectonics on Earth (e.g. Tackley, 1998; Bercovici and Ricard, 2012). They accommodate a large amount of strain and have a direct control on rock rheology, so their development is critical to be addressed to understanding the dynamics of the lithosphere. The formation of viscous shear zones has been considered as resulting from one or several processes of strain-induced weakening, which expresses as a stress drop at constant strain rate or an increase of strain rate at constant stress (e.g. Paterson, 2013). Possible weakening mechanisms include: (1) Geometric and/or (2) fabric softening, (3) a change in deformation mechanism (e.g., due to grain size reduction), (4) fracturing, (5) metamorphic mineral reactions, (6) shear heating (7) water- or (8) melt-induced weakening (e.g. Poirier, 1980; White et al. 1980; Burlini and Bruhn, 2005). While some of these mechanisms apply to monophase rocks, others are more typical of polyphase materials.

As a starting point, laboratory-derived flow laws have been determined for the deformation of monophase materials to understand the rheology of important rock-forming minerals in the viscous regime of the lithosphere, including olivine (e.g., Chopra and Paterson, 1981), quartz (Paterson and Luan, 1990), plagioclase (Rybacki and Dresen, 2000; Dimanov et al., 1999) and pyroxene (Bystricky and Mackwell, 2001). For instance, the experiments of, e.g., Rybacki and Dresen, (2000) and Chen et al., (2006), have shown that water may considerably reduce the strength of aggregates of feldspar and pyroxene. Flow laws and grain size reduction by dynamic recrystallization are also best described in deformation experiments of monophase materials (e.g. White et al. 1980, Schmid 1982, Rutter and Brodie, 1988). These experiments gave rise to a potential source of weakening induced by a transition from grain-size-insensitive to grain-size sensitive creep, but this transition is not expected to occur in monophase aggregates because grain growth is extensive enough at elevated temperature to counteracts the weakening effect of grain size reduction (e.g. De Bresser et al., 2001).

Except for very minor cases, the lithosphere consists of polyphase rocks. Thus, a growing body of literature has also addressed the rheology of polyphase material, given the fact that such a rheology is likely to be different from that of monophase ones (e.g. Bürgmann and Dresen, 2008). The presence of additional phases in polyphase aggregates inhibits grain growth and controls microstructures through pinning (e.g. Olgaard and Evans, 1986; Herwegh et al., 2011). Hence, the dominant deformation mechanism can be expected to differ as a consequence of phase interactions. Of particular interest, the rheology of polyphase aggregates for gabbroic

composition has a fundamental importance for understanding the mechanical behaviour of the oceanic and lower crusts; mafics are the most abundant rock types in these crustal layers (e.g. Weaver and Tarney, 1984; Christensen and Mooney, 1995). However, experimental studies of high-temperature deformation of gabbroic composition are still comparatively rare (e.g. Dimanov et al., 2003, 2007; Dimanov and Dresen, 2005), and none of these studies have considered mineral reactions. They only focused on the role of secondary phases, grain size, water content, stress and spatial distribution of grains to account for changing flow stress and dominant deformation mechanism in polyphase feldspar-pyroxene aggregates. Other studies suggest nevertheless that the occurrence of mineral reactions during viscous flow may have the potential to weaken rocks and consequently localize strain (e.g. Stünitz and Tullis, 2001; De Ronde et al., 2004, 2005; Getsinger and Hirth, 2014; Marti et al., 2017, 2018).

Strain localization and weakening in viscous shear zones as a result of mineral reactions are mostly achieved through changes in P-T conditions (e.g. Gapais, 1989; Newman et al., 1999) or through fluid-rock interactions (e.g. Austrheim, 1987; Menegon et al., 2015). Changes in P-T conditions commonly occur during oceanic and continental subduction and exhumation along crustal-scale shear zones, where the thermodynamic disequilibrium promotes the growth of new stable minerals (e.g. Gerya et al., 2002; Jamtveit et al., 2016). In addition, shear zones represent permeable pathways for fluids that enhance diffusion and strongly catalyse mineral reactions under both, low (e.g. Fitz Gerald and Stünitz, 1993; Newman and Mitra, 1993; Mansard et al., 2018) and high metamorphic grades (e.g. Brodie, 1980; Boundy et al., 1992; Glodny et al., 2003). The importance of mineral reaction lies in the possible grain size reduction and change in deformation mechanism leading to a switch to grain-size sensitive creep, giving rise to substantial weakening (e.g. Etheridge and Wilkie, 1979; Olgaard, 1990; Stünitz and Fitz Gerald, 1993; Fliervoet et al., 1997; De Bresser et al., 1998; Kruse and Stünitz, 1999; De Bresser et al., 2001; Kenkmann and Dresen, 2002; Precigout et al., 2007; Raimbourg et al., 2008; Linckens et al., 2011; Kilian et al., 2011; Viegas et al., 2016). Mineral reactions also contribute to form mixing zones that play an important role of weakening because the pinning of grain boundaries impedes grain growth and keep the grain size small (e.g. Etheridge and Wilkie, 1979; Herwegh et al., 2011).

In this contribution, we investigate the evolution of microstructures in two-phase plagioclase-pyroxene shear experiments, which provide important insights on weakening mechanisms and localization of deformation during shear zone development. This study is an ideal example of how deformation can facilitate metamorphic reactions, heterogeneous

nucleation, formation of fine-grained phase mixtures, and how conversely such an evolution in microstructures eventually results in strain localization and weakening of polyphase aggregates. This also shows the importance of taking into account the behaviour of polyphase assemblages when dealing with the behaviour of the lithosphere.

2. Methods

2.1 Experimental procedure

The shear deformation experiments were carried out in two modified Griggs-type deformation apparatus at the University of Tromsø (Norway) and in a new generation Griggs rig at the University of Orléans (France). The following sections briefly describe the preparation of the sample assembly and experimental procedure.

2.1.1 Starting material and sample preparation

Experiments were performed on two-phase plagioclase-pyroxene assemblages and, for comparison, pure plagioclase and pure pyroxene material. The starting material was prepared from gem-quality Sonora labradorite (An60), and Damaping orthopyroxene from peridotite (Opx: Wo1-En89-Fs10). The initial mineral compositions are presented in Table 1. The rocks were crushed using a hammer and sieved to sizes grains diameter between 100 to 200 µm. Minerals were pre-separated with a Frantz magnetic separator and hand-picked. They were subsequently crushed into an alumina mortar, and then sorted by settling in a distilled water column to extract a powder ranging from 10 to 20 µm grain size. Orthopyroxene and plagioclase powders were mixed at a ratio of 50 : 50% (by volume) as a slurry in acetone using an ultrasonic stirrer to avoid density/grain size separation (De Ronde et al., 2004, 2005). (*insert Table 1*).

The mixed powder was placed between 45° pre-cut alumina forcing blocks (Fig. 1). An amount of ~0.12 g powder for 6.33 mm diameter samples (at Tromsø University) or 0.25 g for 8 mm diameter samples (at Orléans University) were used with 0.1 wt. % H_2O added, so that we end up with a shear zone of ~1 mm thick. A nickel foil of 0.025 mm thickness was wrapped around the pistons and all inserted into a weld-sealed platinum jacket. NaCl was used as solid confining medium and the temperature was controlled by S-type (Pt/Pt-Rh) thermocouples. Detailed descriptions of the sample assembly in the Griggs-type deformation apparatus are given in Pec et al., 2012, Marti et al., 2017 and Précigout et al., 2018. (*insert Fig. 1*).

150 *2.1.2 Experiments*

151 Samples were deformed at constant shear strain rate of ~10^{-5} s^{-1} to varying amounts of
152 shear strain (see Table 2 for a summary of experimental conditions). Pressures and temperatures
153 were increased alternatingly over several hours to achieve the target values of 800, 850, and
154 900°C and confining pressures of 1.0 GPa (Précigout et al., 2018). At the desired P-T
155 conditions, a period of hydrostatic hot-pressing was applied. The deformation part of the
156 experiment was started by advancing the deformation piston first through the lead piece and
157 then touching the upper forcing block (hit point), indicating the starting point of sample
158 deformation. The displacement of the deformation piston within the lead piece is characterized
159 by a slow increase of differential stress ('run-in' curve; Précigout et al., 2018), which has a
160 different duration depending on the experiment. Thus, we separated the experiments with a
161 relatively short (< 65h) and long (> 70h) "run-in" period. Following this period, samples were
162 deformed to shear strains of up to $\gamma = 8$ (high shear strain experiments). Several experiments
163 were also carried out without deformation (hot-pressing experiments) or with deformation only
164 up to the peak stress at $\gamma \approx 1$ (peak stress experiments) in order to study the early stages of
165 deformation. (*insert Table 2*).

166 When deformation was stopped, samples were quenched to 200 °C within minutes
167 (temperature drop of ~150 to 300 °C/min) to preserve the deformation microstructures.
168 Subsequently, the force and confining pressure were decreased simultaneously to room pressure
169 and temperature conditions. During initial stages of the decompression, the differential stress is
170 kept above the confining pressure (~ 100 to 200 MPa) to prevent the formation of unloading
171 cracks. After the experiment, the samples were impregnated with epoxy resin and sectioned
172 along the piston axis for thin sections.

173 Experimental data were digitally recorded using catman® Easy and processed using a
174 MATLAB-based program inspired from the "rig" program of Dr. Matej Pec (Pec et al., 2016)
175 and available at https://sites.google.com/site/jacquesprecigout/telechargements-downloads.
176 The hit point was defined by curve fitting and the stress-strain curves of the deformed samples
177 were then generated by applying corrections on the displacement and force curves considering
178 the rig stiffness and friction of the apparatus, respectively. Furthermore, the sample compaction
179 and surface change (pistons overlap) were corrected to the displacement over the whole period
180 of sample deformation.

181

2.2 *Analytical procedure*

After the experiment, samples were cut along the piston axis in the plane of maximum displacement and vacuum-impregnated with low viscosity epoxy to prepare thin sections for microstructural analysis. The samples were mainly analysed using light and scanning electron microscopy (SEM – TESCAN MIRA 3 XMU) at the ISTO-BRGM (Orléans, France). Starting mineral compositions were determined using electron microprobe CAMECA SX Five (EPMA) at the ISTO-BRGM (Orléans, France) on carbon-coated thin sections (20 nm thickness) at 12 or 15 kV and a beam size of ca. 1 µm.

2.3 *Microstructural analysis*

Grain shape preferred orientations (SPO) were analysed from manually produced bitmaps images using the autocorrelation function (ACF; Panozzo, 1983; Heilbronner, 2002). Since individual grain boundaries are difficult to distinguish, the ACF is used because it does not require segmentation of the individual grains. Thus, this method avoids errors and biases caused by the identification of individual grains. The ACF was calculated both for all the phases combined together (bulk ACF) and for each phase individually (local ACF). For further details about equations related to the ACF, the reader is invited to consult the original study of Heilbronner (1992).

Scanning electron microscope/backscattered electron (SEM/BSE) images were used to produce manually digitized grain maps, which allowed the analysis of grain size. The grain size was defined as the equivalent circular area diameter (Li et al., 2005), and measured using the public domain software ImageJ (http://rsb.info.nih.gov/ij/).

3. Results

3.1. Mechanical data

The terminology used to describe stress-strain curves is explained in Fig. 2a. The same color code is used for different temperatures, and a cross indicates when the forcing blocks started to slip at the sample interface.

3.1.1 Pure plagioclase and pyroxene samples

The pure plagioclase experiments at 800 °C and 900 °C show similar types of stress-strain curves. At 800 °C the sample shows more than 200 MPa higher flow stress than the sample deformed at 900 °C (Fig. 2b), and both samples deform at stresses below the Goetze criterion. The Goetze criterion ($\Delta\sigma \leq P_{conf}$) is used as an empirical criterion to delineate stress conditions where rocks deform plastically (Kohlstedt et al., 1995). In both experiments, the differential stress slightly decreases after reaching a peak stress at $\gamma < 1$ (Fig. 2b). The pure pyroxene experiment with a larger initial grain size fraction (powder sieved to extract a grain fraction $\leq$ 40 µm) is very strong at 900 °C, reaching a peak stress of ~1600 MPa at γ ~0.6, well above the Goetze criterion (Fig. 2b). The experiment was stopped during the stress drop as only brittle deformation was expected to occur at these high differential stresses.

3.1.2 Plagioclase - pyroxene mixtures

The experiments on phase mixtures can be divided into two different series depending on the time spent at P-T conditions before the contact between the σ_1 piston and top alumina piston (hit point). After a short "run-in" period (< 65h at temperature and pressure conditions before hit point), the pyroxene + plagioclase (Opx + Plag) mixtures are very strong at 800 °C (559NM) and 850 °C (557NM), reaching a peak stress of ~ 1100 MPa at γ ~ 0.3 (Fig. 2c). Then, $\Delta\sigma$ drops suddenly far below the Goetze criterion due to slip at one of the sample/forcing block interfaces. The samples deformed at 900°C show peak stress values close to those at 800 and 850 °C, but for higher shear strain (γ ~1.5). At 900 °C, there is a gradual and pronounced weakening after peak stress. In one case, slip occurs at the forcing block interface, and the differential stress decreases below the Goetze criterion before stabilizing around 800 MPa (OR49NM). In the other case, the sample weakens continuously with a reduction of ~50% in

differential stress, until reaching a quasi-steady-state shear stress around 550 MPa near $\gamma \sim 6.5$ (OR41NM). (*insert Fig. 2*).

After a longer "run-in" period (> 70h at temperature and pressure conditions before the hit point), the Opx + Plag mixtures show a less steep loading curve compared to shorter run-in period experiments (Fig. 2d), indicating a lower strength of the samples (the loading curve in the solid-medium apparatus at high temperatures is not a purely elastic, but involves a component of permanent sample strain; Richter et al. 2018). At 800 °C, a stress drop occurs at a peak stress value near $\gamma \sim 0.7$ (above the Goetze criterion at ~1250 MPa), probably caused by slip at one sample-forcing block interface (OR24NM). In contrast, the other samples at 850 °C (OR38NM) and 900 °C (OR34NM) weaken continuously after peak stress, and then approach a quasi-steady-state shear stress at $\gamma \sim 7.8$ and $\gamma \sim 6$, respectively (Fig. 2d). In these last 2 experiments, the weakening is very pronounced with ~64 % of weakening for the 850 °C sample and ~78 % for the 900 °C sample compared to peak stress values.

These sets of experiments (Fig. 2) demonstrate that pure phase samples are either very strong and deform only in the brittle field (Opx), or relatively weak and deform plastically (Plag) at a moderate to low flow stress without significant weakening after peak stress. The initial strength of mixed phase samples (peak stress) lies between the two extreme values of the pure phase samples, but the mixed phase samples weaken after peak stress and give rise to a final strength far weaker than the weakest of our mono-phase samples (i.e., pure plagioclase).

3.2 Microfabrics and composition

3.2.1 Pure end-members experiments

The pure Plag samples deformed at 800 °C and 900 °C are microstructurally similar to one another and show homogeneous deformation. Although it is difficult to distinguish all individual plagioclase grains in BSE images, there is clear plagioclase grain size refinement locally (Fig. 3a). Recrystallized grains do not show different chemical composition with respect to the relict grains. While our experiments are stronger than those carried out by Stünitz and Tullis (2001), the microstructures are similar and no reaction products are formed at the P-T conditions imposed.

The pure Opx sample with larger initial grain size ($\leq$ 40 µm) deformed at 900 °C shows extensive fracturing, indicative of brittle deformation (Fig. 3b). The pervasive fractures result

in a locally dramatically reduced pyroxene grain size (down to < 1 μm; Fig. 3c). No indication for plastic deformation was detected. (*insert Fig. 3*).

3.2.2 Mixed phase samples

3.2.2.1 High shear strain samples

3.2.2.1.1 General features

At 850 °C, the high-strain sample is characterized by a single high strain zone that traverses the sample through the centre from one interface of the forcing block to the other (Fig. 4). The reaction products appear pervasively in the whole sample, but the high-strain zone contains considerably more reaction products (~80%) than the low-strain one (~28%). The grain size of the reaction product also substantially reduces in the high-strain zone with respect to the low-strain regions. In this latter, the reaction product develops as coronas at the Opx_1-$Plag_1$ boundaries, or as monophase aggregates without the development of mixed phase zones (Fig. 5a). This reaction product is identified as newly-formed pyroxene (Opx_2), plagioclase ($Plag_2$) and amphibole (Amph); all of which were absent from the starting material. The original Opx_1 clasts are locally cut by brittle fractures, reducing slightly the grain size (Fig. 5b) and the fractures are filled with Opx_2 reaction products. The transition between low-and high-strain zones can locally be gradual and shows the incipient mixing of phases at the edges of original Opx_1 (Fig. 5c-d). The reaction progressively consumes the pre-existing Opx_1 and induces the development of σ-tails parallel to the shear direction. These tails locally coalesce and form interconnected shear bands of fine-grained reaction products composed of Opx_2, $Plag_2$ and locally Amph, which usually have rounded grain shapes (Fig. 5c-d). (*insert Fig. 4*).

3.2.2.1.2 High-strain zones

Reactions in high-strain zones result in intense grain size reduction and in coalescence of foliation-forming layers of fine grains parallel to each other into mixed phase shear bands, usually laterally connected and subparallel to the shear direction (Fig. 5e-f, 6). Some of the shear bands have a synthetic orientation with respect to the bulk shear zone (C′-type orientation in the sense of Berthé et al., 1979), others are parallel to the shear direction (C-type orientation). At 850 °C, the majority of shear bands are organized within high-strain zones of ~250-300 μm

thick (Fig. 6a-b). Similar features are shared at 900 °C, although deformation is more distributed (Fig. 6c-d-e). (*insert Fig. 5*).

The modal proportion of reaction products reaches locally 80% in the high-strain zones, as these products replace most of the pre-existing large grains, including the original $Plag_1$ (Fig. 7a). Thus, most of the fine-grained mixed phase shear bands are composed of reaction product (Opx_2, $Plag_2$ and Amph). The high-strain zones still comprise some original Opx_1 clasts that are embedded in the fine-grained reaction product (Fig. 5e), but these clasts are reduced in size (from reaction) and appear less elongated and more disoriented compared to those of the low-strain zones (Fig. 7b). The Opx_1 appears therefore as a mechanically rigid clast within weaker mixing zones composed of reaction product, the grain size of which is typically below one micron. (*insert Fig. 6*).

There is a gradient in the aspect ratio and the orientation of reaction product between low- and high-strain zones. The bulk aspect ratio is higher in the high-strain zones, where the amount of reaction product is the most abundant (Fig. 7). Moreover, the bulk aspect ratio is around one and a half times higher in the high-strain zones compared to the low-strain ones. The reaction product in the high strain zones is also strongly oriented subparallel to the shear plane (piston interface (Fig. 7d; α between ~ 3° and 5°). In the low strain zones, the reaction product is less oriented (Fig. 7d; $\alpha \sim 9°$). By applying the equation that relates the preferred orientation of passive lines with respect to the shear plane ($\gamma = 2/\tan 2\theta$; Ramsay, 1980), we can estimate that local shear strain reaches γ ~11 to 16 in the high-strain zones and $\gamma \sim 6$ in the low-strain ones. (*insert Fig. 7*).

3.2.1.2.3 Mineral chemistry

Overall, major compositional changes in plagioclase and pyroxene are coeval with grain size reduction in sample shear zones (Fig. 8a-b). The chemical composition of new grains of plagioclase and pyroxene distinctly differs from that of relict clasts. While the chemical composition of clasts is mostly An59, the new reaction rim ($Plag_2$) is more albitic (An52; Fig. 8a). The reaction also results in almost complete disappearance of $Plag_1$ in the high-strain zones (Fig. 7a), and within mixed phase zones and shear bands, the anorthite component of fine-grained $Plag_2$ is slightly lower than that of new rims (An49).

Pyroxene has the same chemical evolution relationship between relict clasts and new rims (Fig. 8b). The chemical composition of clasts (Opx_1) varies from En(86) to En(90), while the rim composition (Opx_2) shows a decreasing enstatite content down to En(82). The composition of fine-grained new Opx2 in the high-strain zone decreases even more to En(79). The reaction product thus characterizes by an enrichment in iron content, together with the formation of new amphibole grains enriched in Mg and depleted in Fe. These syn-kinematic amphibole appears in both, more and less deformed zones, but they are more abundant in fine-grained shear bands and in the sample deformed at 850 °C. Based on large grains composition in the low-strain zones – the grain size is too fine in shear bands of the high-strain zones to distinguish individual grains and measure the composition –, amphiboles are essentially classified as magnesio-hornblende and tschermakite (Fig. 8c). (*insert Fig. 8*).

3.2.2 Hot-pressing and peak stress experiments

Some samples were hot-pressed (without deformation) for the same duration as the high shear strain samples for comparison of microstructure and reaction progress. Hot-pressing samples of Opx + Plag at 900 °C show the development of reaction product (Fig. 9a-b), which have the same composition of Opx_2, $Plag_2$ and Amph in the deformed samples. The reaction product only occurs as thin coronas at the Opx_1-$Plag_1$ phase boundaries. The volume of reaction product reaches about 3% in the sample held for 100h and about 10% in the one held at the same pressure and temperature for 193h. Except from this increase in reaction product, there is no difference between the two hot-pressing samples.

In samples where the deformation was stopped at peak stress, the microstructures differ slightly in the amount of reaction product and their arrangement with respect to the microstructures of the hot-pressing experiments (Fig. 9c-d). Indeed, the amount of reaction product slightly increases in peak stress experiments compared to the hot-pressing ones. The reaction product is relatively homogeneously distributed in the samples, although it starts to coalesce locally and forms partially connected layers (Fig. 9d). The original Opx_1 and $Plag_1$ grains are also slightly elongated in the flow direction. When these experiments reach relatively high conditions of differential stress, close to the Goetze criterion, fractures locally affect the pyroxene and cause a slight reduction in grain size. (*insert Fig. 9*).

363 *3.2.3 Intermediate shear strain experiment*

364 In our set of experiments, one sample was taken to a more or less intermediate strain
365 and is considered as a transient sample between peak stress and high shear strain experiments
366 (Fig. 2c; OR49NM). This sample is characterized by the development of subparallel fine-
367 grained polyphase layers or shear bands (Fig. 10a), both composed of an intimate mixture of
368 extremely fine-grained Opx_2, $Plag_2$ and Amph (Fig. 10b). The layers and shear bands originate
369 from tails that extend from the edges of original Opx_1 (Fig. 10c), and progressively coalesce to
370 form an interconnected network (Fig. 10a). (*insert Fig. 10*).

371

372 *3.3 Grain size*

373 The overall grain size for both plagioclase and pyroxene grains is strongly reduced with
374 increasing strain. Most of the pyroxene grain size reduction occurs after the peak stress, and
375 hence, during the weakening and development of fine-grained mixed phase zones (Fig. 11).
376 While the pyroxene grain size remains almost unchanged at peak stress with respect to the
377 starting material (only cracking refines the grain size to a mode of 15.6 μm), it strongly
378 decreases in mixed phase zones at high shear strain (mode of distribution = 0.2 μm). To ensure
379 accurate grain size determination, we have excluded plagioclase from the measurements
380 because of the difficulty to distinguish individual grains in plagioclase aggregates. Despite this
381 issue, visual inspection suggests that the plagioclase grain size in stable fine-grained mixtures
382 is similar to that of pyroxene. (*insert Fig. 11*).

383

384 *3.4 Reaction progress*

385 The set of experiments performed at different durations and 900 °C is used to illustrate
386 the relation between the volume fraction of reaction product with time and the effect of
387 deformation on reaction (Fig. 12). The volume fraction of reaction product increases from ~3%
388 for 100h to ~10% at 193h if deformation is not applied (OR55NM and OR43NM) (Fig. 12a).
389 In contrast, even after a short period of deformation to small strain at peak stress, the volume
390 fraction of reaction product increases to ~11% (OR51NM) and ~18% (OR47NM) (Fig. 12a).
391 This amount of reaction product is higher than the amount documented for the hot-pressing
392 experiment with equivalent duration. Thus, the influence of deformation on the amount of
393 reaction product is higher than the influence of time. This influence has an effect on the strength

of the deformed assemblages, as the more reaction product they contain, the weaker they are (Fig. 12b). The deformed and undeformed samples therefore significantly differ in terms of Avrami relationship, i.e., in terms of reaction progress without incubation time before the hit point (Fig. 12b). (*insert Fig. 12*).

4. Discussion

4.1 Mechanical data

The mechanical data of our experiments show a systematic difference in the rheological evolution between monomineralic samples (opx or plag) and phase mixtures (Fig. 2): The monomineralic samples either deform by brittle mechanisms only (opx; the experiment was stopped before failing completely), or they deform viscously at steady state stresses following a weakening of less than 150 MPa (plag). The deformation of pure Opx also gives rise to high differential stress at 900 °C ($\Delta\sigma$ ~1600 MPa; Fig. 2b). Advances in rock deformation studies provided detailed documentations about the creep behaviour of pyroxene (e.g. Bystricky and Mackwell, 2001; Dimanov et al., 2003, 2005; Chen et al., 2006), but mostly for CPx; the mechanical behaviour of Opx remains very limited (Bruijn and Skemer, 2014; Bystricky et al., 2016). The comparison of Opx mechanical results and estimated strain rates for wet Cpx, by applying the flow law of Dimanov and Dresen (2005), suggest that the Opx strength is higher compared to that of the Cpx (Fig. 13a). For pure Plag, our flow stresses at the given strain rate for $\gamma > 2$ (= steady state conditions) are in good agreement (Fig. 13b) with the flow law by Rybacki and Dresen (2000) using the conversion between simple shear and coaxial strain rates of $\dot{\varepsilon} = \dot{\gamma} / \sqrt{3}$ (Tokle et al., 2019). Our results for pure phase Plag and Opx are thus quite consistent with previous results found in the literature.

The mixture samples deform under continuous weakening after attaining a peak stress that is intermediate between the end-member strengths of Opx and Plag, strength of which is consistent with a Reuss-Voigt- or Taylor-Sachs models (e.g., Dimanov and Dresen, 2005). However, the Opx in our case appears to be stronger than Cpx and deforms only by brittle processes, so that the peak strength of the 2-phase composite sample is between the two end-members and near the Goetze criterion (Fig. 2). In addition, the pronounced weakening after peak stress produces final flow stresses that are far below (up to 800 MPa) the Goetze criterion ($\Delta\sigma \leq P_{conf}$) nearby the strength of the weaker end-member phase. This suggests that the deformation mechanism of the phase mixture differs from those of the end-members.

Otherwise, the strength of the composite would lie between the end-member strengths of a Reuss-Voigt or Taylor-Sachs-model. As discussed below, such a different rheological evolution may be explained by the progressive modification of the phase assemblage and microstructure through chemical interactions, i.e., mineral reactions. (*insert Fig. 13*).

4.2. Nucleation and grain size reduction

From figures 4 to 7, the local zones of reaction product accommodate far more strain than the relict phases Opx and Plag, so that the reaction product is responsible for the mechanical weakening of the samples. In addition, the microstructures at peak stress conditions mainly consist of coronas with only incipient mixed phase zones (Fig. 9c-d), and hence, most of the phase mixing starts after the peak stress. Reaction product also has a very small grain size (Fig. 11). As the intense grain size reduction and phase mixing start to appear both after peak stress (Fig. 14), strain weakening and partitioning into high-strain zones (Fig. 6) likely commence as a consequence of these processes.

Although there is no flow law for Plag + Opx mixtures and composite flow laws only exist for Cpx + Plag (Dimanov and Dresen, 2005), we plotted the measured grain size modes of the fine-grained reaction product (Opx + Plag) into the existing Cpx and Plag deformation mechanisms maps for a semi-quantitative comparison. The observed grain sizes of Opx at the final strength of the composite phase mixtures plot into the diffusion creep field at the nominal applied strain rates of the samples (Fig. 13), whereas the Plag at the same grain size yields an order of magnitude of higher strain rates. Because of strain partitioning, the expected strain rates in the high-strain zones are higher than the bulk ones by a factor of 2 to 3. Thus, the strain rates of the Plag - Opx mixtures are in the range of the Cpx strain rates and slower than the predicted ones for Plag in the diffusion creep field (Fig. 13).

Several processes are generally invoked to account for phase transformations that may reduce grain size and promote phase mixing, influencing the rock strength. Some workers proposed that melt reactions may strongly influence the mechanical behaviour of rocks of the lower crust by inducing phase mixing and introducing a low viscosity melt in the system (e.g. Rosenberg and Handy, 2005). In our case, the P-T conditions imposed to the Opx + Plag system are definitely outside of the melt-forming field, in agreement with the lack of melt in our samples. Another weakening process may involve dynamic recrystallization in the regime 1 of Hirth and Tullis (1992), i.e., if recrystallization mostly occurs by bulging, but dynamic

458 recrystallization does not produce phase mixing, and the pyroxene grain size in zones of mixed
459 phase reaction products falls far below the orthopyroxene piezometer (Fig. 13; Linckens et al.,
460 2014). The new Opx_2-grains also have a different chemical composition compared to the
461 starting material (Fig. 8), which excludes fracturing as a source of extensive grain size
462 comminution (e.g. Ree et al., 2005; Park et al., 2006; Pec et al., 2012, 2016). In low-strain zones
463 of samples that reach high differential stress conditions, discrete fractures affect Opx_1 clasts,
464 inducing their breakdown into smaller fragments but not to extensive size comminution. In
465 contrast, phase nucleation and a switch to grain size sensitive dissolution-precipitation creep
466 has been described in previous studies (e.g. Kilian et al., 2011; Herwegh et al., 2011; Wassmann
467 and Stoeckhert, 2013; Hidas et al., 2016; Précigout and Stünitz, 2016; Marti et al., 2018; Prigent
468 et al., 2018). As typically associated with metamorphic reactions (e.g. De Ronde et al., 2004,
469 2005), such a phase nucleation may account for changing chemistry and phase mixing during
470 extensive grain size reduction in our experiments. (*insert Fig. 14*).

471

472 *4.3 Mineral reaction and dissolution-precipitation creep*

473 While the development of reaction coronas induces limited grain size reduction and no
474 phase mixing in low-strain zones (Fig. 5a-b, 14), the grain size reduction is much more intense
475 in high-strain zones, combined with phase mixing (Fig. 5e-f, 6, 14). At the margin of high-
476 strain zones, the early stages of phase mixing are preserved (Fig. 5c-d, 14). Fine-grained layers
477 composed of Opx_2, $Plag_2$ and Amph extend at the edges of Opx_1 clasts and progressively replace
478 the original $Plag_1$ (Fig. 5c-d). The mixing starts at the edges of the original Opx_1 that is gradually
479 dissolved as evidenced by irregular grain boundaries, where new grains nucleate in some
480 localities along low-stress sites of Opx_1 grain boundaries (Fig. 5c). These microstructures
481 suggest that diffusion mass transport takes place and facilitates dissolution – precipitation creep.
482 Previous studies also showed that phase nucleation forming tails at the expense of clasts may
483 increase the degree of mixing in natural shear zones (e.g. Kruse and Stünitz, 1999; De Ronde
484 et al., 2004, 2005, Holyoke and Tullis, 2006a, b, Kilian et al., 2011, Mansard et al., 2018).
485 In our experiments, the nucleation of small phases causes an irreversible effect on the
486 deformation processes because no grain growth is observed with increasing strain or larger
487 duration of the experiments. The mixing of phases causes pinning of grain boundaries and
488 impedes grain growth, so the fine grain size of the mixed phase zones is preserved (e.g. Fliervoet
489 et al., 1997; Herwegh et al., 2011; Kilian et al., 2011, Platt, 2015). Therefore, the nucleation of

fine-grained mixed phase layers is an efficient mechanism to maintain deformation of weak material.

One important accommodation process in diffusion creep is grain boundary sliding (e.g, Langdon, 2006). In a reacting and simultaneously deforming mineral assemblage, it has a two-fold effect: it creates new contact surfaces for reaction and it produces potential cavitation sites, where new phases can nucleate (e.g., Kilian et al., 2011, Menegon et al., 2015, Précigout and Stünitz, 2016; Précigout et al., 2017). In this way, phase mixing is promoted, in agreement with 1) the heterogeneous nucleation of fine grains (Fig. 11), 2) the relatively well-mixed phases in high-strain zones (Fig. 5e-f, 6), and 3) the fact that pyroxene and plagioclase grain size in these zones falls within the diffusion creep field (Fig. 12). The significant weakening and strain localization during deformation is consistent with the increase in strain rate (e.g. Schmid et al., 1980, Rutter and Brodie, 1988; Montési, 2007; Precigout et al., 2007; Raimbourg et al., 2008; Gueydan et al., 2014). Due in particular to the dominance of diffusion creep and the occurrence of weakening resulting in strain localization, the fine-grained high-strain zones constitute the parts of the sample that weaken the most.

4.4 Geometrical aspects: connectivity of shear zones and weakening processes

Previous works have shown that rheological behaviour of rocks and strain localization can be highly dependent on strength contrast between phases, spatial geometry and amount of mineral reactions (e.g. Handy, 1990; Dell'Angelo and Tullis, 1996; Holyoke and Tullis, 2006a; Hansen et al., 2012). Holyoke and Tullis (2006a) found in high-temperature experiments a strong relation between interconnection of weaker phases and strain localization. It has also been shown by the studies of, e.g., Pec et al., (2016) and Palazzin et al., (2018) that the bulk strength of samples remains high if the weak layers are not simply connected. Numerical studies also support the idea that phase arrangement can dramatically affect the bulk strength (e.g. Montési, 2007, Montési, 2013; Gerbi et al., 2016).

In our study, the fine-grained layers are well connected and oriented sub-parallel to the shear plane, suggesting that the reaction product is connected in three dimensions and therefore controls the bulk strength of the sample. This arrangement is considered as a type of geometric weakening (e.g. Handy, 1994; Dell'Angelo and Tullis, 1996; Holyoke and Tullis, 2006a; Gerbi et al., 2016). In addition, reaction progress will introduce more of the weak fine-grained material, increasing the probability of the reaction product to form connected layers after peak stress, and hence, to pronounce further weakening. Previous simple-shear studies also revealed

523 the formation of shear bands after peak stress (e.g. Holyoke and Tullis, 2006a; Pec et al., 2016;
524 Marti et al., 2018). However, unlike our study, they do not always show the localization of
525 shear bands into broad and highly localized high-strain zones, that are connected through the
526 shear zone in the high shear strain experiments (Fig. 4).

527 Our results support the idea that the samples weakening is dependent on two processes:
528 (1) the introduction of fine-grained reaction product, and (2) its connectivity, which should
529 increase with an increasing amount of reaction product, but not necessarily. We thus conclude
530 that the weakening of the samples is caused by the connectivity of reaction product, so that the
531 proportion and arrangement of weak materials evolve first into highly localized and thin fine-
532 grained polyphase layers in the intermediate strain parts, and then into connected broader high-
533 strain zones in high strain samples (Fig. 14). The bulk weakening is only achieved when the
534 weak layers are interconnected.

535

536 *4.5 Influence of deformation on reactions*

537 A common response to the effect of deformation on solid-state chemical reactions is that
538 the deformation may enhance the kinetics of mineral reactions (e.g. Yund and Tullis, 1991;
539 Wintsch et al., 1995; Baxter and De Paolo, 2004; Imon et al., 2002; Yonkee et al., 2003;
540 Holyoke and Tullis, 2006; De Ronde and Stunitz, 2007, Richter et al., 2016). In our high-strain
541 samples, we document a strong localization of deformation into high-strain zones (Fig. 4). The
542 fact that the reaction product constitutes much of the high-strain zones at 850 and 900°C (Fig.
543 7a) strongly argues in favour of reaction kinetics enhanced by deformation. This deformation-
544 reaction feedback is more pronounced at 850°C, as the amount of syn-kinematic amphiboles
545 formed in high-strain zones is higher. A similar feedback was found in sheared plagioclase-
546 olivine experiments at 900°C (De Ronde and Stünitz, 2007), and they showed that the local
547 strain is highly correlated with reaction progress. Recently, Marti et al., (2018) also described
548 the positive feedback between deformation and reaction progress in experimentally deformed
549 plagioclase-pyroxene mixtures, but with less reaction product. The greater reaction progress
550 and larger amount of fine-grained mixed phase zones in our samples may be attributed to the
551 small grain size of our starting material in otherwise very similar experimental procedures as
552 Marti et al., (2018). The partially smaller grain size in our samples provides a greater surface
553 area of phase boundaries as sites of potential reactions.

554 The evidence that deformation affects reaction kinetics comes from the comparison of
555 hydrostatic hot-pressing samples, the deformed samples to peak stress, and to higher shear
556 strain (Fig. 12a). The main difference between these samples is the bulk amount of reaction
557 product. The comparison of hot-pressing samples held at 900°C and 1 GPa for a different period
558 of time (~100h and 193h) reveals a slight increase in the amount of reaction product with time
559 (Fig. 12b). Similarly, the comparison of two deformed samples to peak stress that reached
560 similar shear strain for a different period of time (~85h and 200h) only shows a slight increase
561 of reaction product (Fig. 12b). This difference in incubation time before deformation, however,
562 is potentially important in terms of rheological behaviour. The longer the incubation time before
563 the hit point, the greater the volume of reaction product, and the weaker is the sample at peak
564 stress (Fig. 2, 12a-b). Nonetheless, the comparison of hot-pressing and peak stress samples with
565 a similar period of time reveals that the influence of time on the amount of reaction product is
566 minor compared to the effect of deformation (Fig. 12b).

567 Although 2 data points for hot-pressing samples are not sufficient to establish an
568 accurate Avrami relationship, an Avrami curve is fitted for comparison with other samples (Fig.
569 12). The initial slow reaction progress in hydrostatic samples compared to deformed samples
570 (without the incubation time) is obvious (Fig. 12c). With increasing strain, there clearly is a
571 greater volume of reaction product. Similar results have been documented in experimentally
572 deformed fine-grained gneiss (Holyoke and Tullis, 2006 a, b) and plagioclase + olivine samples
573 (De Ronde and Stunitz, 2007). The main reason for the faster reaction progress in deformed
574 samples is probably the introduction of defects into the reactants, i.e. the increase of the
575 activation energy for the reaction at otherwise identical pressure and/or temperature
576 overstepping conditions (De Ronde and Stunitz, 2007).

577

578 *4.6 Geological application – shear localization in nature*

579 In our deformation experiments the starting material Opx + Plag was deliberately chosen
580 to be out of equilibrium at the experimental pressure and temperature conditions. In nature, P-
581 T conditions change occur at lower rates, potentially inducing progressive changes in mineral
582 assemblages (e.g. Herwegh et al., 2011). However, cases of preserved metastable mineral
583 assemblages in undeformed rocks are well documented, while deformed equivalents of the
584 same rock body have reacted (e.g. Austrheim and Griffin, 1985, Koons et al., 1987, Früh-Green,
585 1994). Thus, mineral reaction and its interplay with deformation is of great importance in nature

(e.g. Kerrich et al., 1980; Brodie and Rutter, 1985; Handy and Stünitz, 2002; Keller et al., 2004; Mansard et al., 2018). Indeed, it has been shown by the study of, e.g., Keller et al., 2004 that the extent of metamorphic reactions is greater in shear zones, as reaction may cause strain localization by producing a mechanically weak aggregate. This shares similarities with natural studies showing that strain and mineral reactions are intimately linked and influence each other (e.g. Mitra, 1978; Brodie and Rutter, 1985; Whitmeyer and Wintsch, 2005). Thus, the investigated polyphase mixture is a good analogue to natural shear zones involving strain-enhanced chemical reactions and reaction-enhanced strain weakening, although large overstepping of reaction boundary may occur in our experiments.

It is now well established that the lower crust is lithologically heterogeneous, mainly consisting of mafic rocks dominated by feldspar and pyroxene (e.g. Kirby and Kronenberg, 1987; Christensen and Mooney, 1995; Rudnick and Fountain, 1995). Experimental investigations on the rheology of feldspar (e.g. Rybacki and Dresen, 2000; Dimanov et al., 2003), pyroxene (e.g. Bystricky and Mackwell, 2001), and polyphase assemblages of feldspar and pyroxene (Dimanov and Dresen, 2005) reveal that these two phases are mechanically strong, although pyroxene is 1-2 orders of magnitude stronger than feldspar under dry conditions (e.g. Dimanov and Dresen, 2005). Our study also demonstrates that Opx + Plag assemblages are strong, but as soon as these assemblages react, the sample is viscously deformed and the strength weaken. Indeed, the deformation of Opx + Plag assemblages promotes diffusion-controlled chemical reactions which induce the nucleation of new intrinsically strong phases, i.e., plagioclase and pyroxene (Fig. 2a). However, these strong phases nucleate as fine grains within weak mixed phase zones (Fig. 6, 11), causing a switch in deformation mechanism, and thereby extending the range of conditions where the fine-grained mixed zones are weaker than the unreacted assemblages. Several workers pointed out that such localization of strain in weak layers may control the degree of weakening in polyphase rocks (e.g. White et al., 1980; Handy, 1989). This is of great importance in the comprehension of the rheological behavior of the lower crust, because a large amount of fine-grained weak zones allows to preserve the weak long-term behaviour of a shear zone in the lower crust. Thus, the rheology of polyphase assemblages is controlled by many factors, including mineral reactions, grain size reduction and strain partitioning. The effect of these processes related to the complex interaction between plagioclase and pyroxene on lower crust rheology are however not taken into account in the current lithospheric models. These models should consider mechanical

polyphase layers to describe the lower crust, as it has been shown in natural lower-crustal shear zones (e.g. Kanagawa et al., 2008; Kruse and Stünitz, 1999).

5. Conclusions

In this study, we have performed rock deformation experiments on plagioclase + pyroxene and pure end-member assemblages in Griggs-type deformation apparatus at 1 GPa, and temperatures ranging from 800 to 900°C. The analysis of pure end-member assemblages reveals that in the absence of reaction, only initial strain weakening due to recrystallization occurs in Plag, which then deforms at steady-state stress. And Opx deforms only by brittle mechanisms. In contrast, plagioclase + pyroxene assemblages show extensive strain weakening caused by mineral reactions. These deformed assemblages show the importance of the interaction between deformation and reaction on grain size reduction and phase mixing, leading to strain partitioning and weakening in fine-grained shear zones. This study represents a good analogue to natural shear zones involving mechanical weakening caused by mineral reactions, particularly in mafic rocks. At the onset of deformation, new phases nucleate in aggregates as mixed phase tails and layers at the expense of original pyroxene and progressively replace the original plagioclase. The change of phase composition together with phase mixing indicates that grain size reduction originates from dissolution-precipitation. This suggests that pressure-solution creep may have significantly contributed to weaken the mixture samples. As deformation and reaction progress, thin weak layers coalesce to form simply connected material in high-strain zones. The intense grain size reduction occurring in mixed high-strain zones considerably changes the rheology of the assemblage, and it increases the strength contrast between the weak high-strain zones, able to deform by grain-size sensitive diffusion creep, and the mechanically strong low-strain ones. The interplay between deformation and reaction is responsible for strain partitioning and localization in high-strain zones. The degree of connectivity of the reacted material controls the bulk rheology of the shear zone.

Acknowledgements

This work has received funding from the European Research Council (ERC) under the seventh Framework Programme of the European Union (ERC Advanced Grant, grant agreement No 290864, RHEOLITH), and from the Labex VOLTAIRE (ANR-10-LABX-100-01). The authors are grateful to Sylvain Janiec for the preparation of thin sections, Patricia Benoist and Ida Di-carlo for analytical support, Esteban Le Moing and Frédéric Savoie for technical assistance. We also thank Mark Zimmerman very much for kindly providing the Damaping peridotite material.

References

Austrheim, H., 1987. Eclogitization of lower crustal granulites by fluid migration through shear zones. Earth and Planetary Science Letters 81, 221–232. https://doi.org/10.1016/0012-821X(87)90158-0

Austrheim, H., Griffin, W.L., 1985. Shear deformation and eclogite formation within granulite-facies anorthosites of the Bergen Arcs, western Norway. Chemical Geology 50, 267–281. https://doi.org/10.1016/0009-2541(85)90124-X

Baxter, E.F., Depaolo, Æ.D.J., 2004. Can metamorphic reactions proceed faster than bulk strain ? 657–670. https://doi.org/10.1007/s00410-003-0525-3

Bercovici, D., Ricard, Y., 2012. Mechanisms for the generation of plate tectonics by two-phase grain-damage and pinning. Physics of the Earth and Planetary Interiors 202–203, 27–55. https://doi.org/10.1016/J.PEPI.2012.05.003

Berthé, D., Choukroune, P., Jegouzo, P., 1979. Orthogneiss, mylonite and non coaxial deformation of granites: the example of the South Armorican Shear Zone. Journal of Structural Geology 1, 31–42. https://doi.org/10.1016/0191-8141(79)90019-1

Boundy, T.M., Fountain, D.M., Austrheim, H., 1992. Structural development and petrofabrics of eclogite facies shear zones, Bergen Arcs, western Norway: implications for deep crustal deformational processes. Journal of Metamorphic Geology 10, 127–146. https://doi.org/10.1111/j.1525-1314.1992.tb00075.x

Brodie, K.H., 1980. Variations in mineral chemistry across a shear zone in phlogopite peridotite. Journal of Structural Geology 2, 265–272. https://doi.org/10.1016/0191-

679 8141(80)90059-0

680 Brodie, K.H., Rutter, E.H., 1985. On the Relationship between Deformation and
681 Metamorphism, with Special Reference to the Behavior of Basic Rocks. Springer, New
682 York, NY, 138–179. https://doi.org/10.1007/978-1-4612-5066-1_6

683 Bruijn, R., Skemer, P., 2014. Grain-size sensitive rheology of orthopyroxene. Geo-phys. Res.
684 Lett. 41, 1–10. https://doi.org/10.1002/2014GL060607

685 Bürgmann, R., Dresen, G., 2008. Rheology of the Lower Crust and Upper Mantle: Evidence
686 from Rock Mechanics, Geodesy, and Field Observations. Annual Review of Earth and
687 Planetary Sciences 36, 531–567. https://doi.org/10.1146/annurev.earth.36.031207.124326

688 Burlini, L., Bruhn, D., 2005. High-strain zones: laboratory perspectives on strain softening
689 during ductile deformation. Geological Society, London, Special Publications 245, 1–24.
690 https://doi.org/10.1144/GSL.SP.2005.245.01.01

691 Bystricky, M., Lawlis, J., Mackwell, S., Heidelbach, F., Raterron, P., 2016. Journal of
692 Geophysical Research: Solid Earth. 6384–6400. https://doi.org/10.1002/2016JB013011

693 Bystricky, M., Mackwell, S., 2001. Creep of dry clinopyroxene aggregates. Journal of
694 Geophysical Research: Solid Earth 106, 13443–13454.
695 https://doi.org/10.1029/2001JB000333

696 Chen, S., Hiraga, T., Kohlstedt, D.L., 2006. Water weakening of clinopyroxene in the
697 dislocation creep regime. J. Geophys. Res. 111, B08203.
698 https://doi.org/10.1029/2005JB003885

699 Chopra, P.N., Paterson, M.S., 1981. The experimental deformation of dunite. Tectonophysics
700 78, 453–473. https://doi.org/10.1016/0040-1951(81)90024-X

701 Christensen, N.I., Mooney, W.D., 1995. Seismic velocity structure and composition of the
702 continental crust: A global view. Journal of Geophysical Research: Solid Earth 100, 9761–
703 9788. https://doi.org/10.1029/95JB00259

704 De Bresser, J.H.P., Peach, C.J., Reijs, J.P.J., Spiers, C.J., 1998. On dynamic recrystallization
705 during solid state flow: Effects of stress and temperature. Geophysical Research Letters
706 25, 3457–3460. https://doi.org/10.1029/98GL02690

707 De Bresser, J.H.P., Ter Heege, J.H., Spiers, C.J., 2001. Grain size reduction by dynamic

recrystallization: Can it result in major rheological weakening? International Journal of Earth Sciences 90, 28–45. https://doi.org/10.1007/s005310000149

De Ronde, A.A., Heilbronner, R., Stünitz, H., Tullis, J., 2004. Spatial correlation of deformation and mineral reaction in experimentally deformed plagioclase–olivine aggregates. Tectonophysics 389, 93–109. https://doi.org/10.1016/J.TECTO.2004.07.054

De Ronde, A.A., Stünitz, H., Tullis, J., Heilbronner, R., 2005. Reaction-induced weakening of plagioclase–olivine composites. Tectonophysics 409, 85–106. https://doi.org/10.1016/J.TECTO.2005.08.008

De Ronde, A.A., Stunitz, H., 2007. Deformation-enhanced reaction in experimentally deformed plagioclase–olivine aggregates. Contributions to Mineralogy and Petrology 153, 699–717.

Dell'Angelo, L.N., Tullis, J., 1996. Textural and mechanical evolution with progressive strain in experimentally deformed aplite. Tectonophysics 256, 57–82. https://doi.org/10.1016/0040-1951(95)00166-2

Dimanov, A., Dresen, G., Xiao, X., Wirth, R., 1999. Grain boundary diffusion creep of synthetic anorthite aggregates: The effect of water. Journal of Geophysical Research: Solid Earth 104, 10483–10497. https://doi.org/10.1029/1998JB900113

Dimanov, A., Dresen, G., 2005. Rheology of synthetic anorthite-diopside aggregates: Implications for ductile shear zones. Journal of Geophysical Research 110, B07203. https://doi.org/10.1029/2004JB003431

Dimanov, A., Lavie, M.P., Dresen, G., Ingrin, J., Jaoul, O., 2003. Creep of polycrystalline anorthite and diopside. Journal of Geophysical Research: Solid Earth 108. https://doi.org/10.1029/2002JB001815

Dimanov, A., Rybacki, E., Wirth, R., Dresen, G., 2007. Creep and strain-dependent microstructures of synthetic anorthite–diopside aggregates. Journal of Structural Geology 29, 1049–1069. https://doi.org/10.1016/J.JSG.2007.02.010

Etheridge, M.A., Wilkie, J.C., 1979. Grainsize reduction, grain boundary sliding and the flow strength of mylonites. Tectonophysics 58, 159–178. https://doi.org/10.1016/0040-1951(79)90327-5

Etheridge, M.A., Wilkie, J.C., 1979. Grainsize reduction, grain boundary sliding and the flow strength of mylonites. Tectonophysics 58, 159–178. https://doi.org/10.1016/0040-

738 1951(79)90327-5

739 Fitz Gerald, J., Stünitz, H., 1993. Deformation of granitoids at low m~tamo~~ic grade. I:
740 Reactions and grain size reduction. Elsevier Science Publishers B.V 221, 269–297.
741 https://doi.org/10.1016/0040-1951(93)90164-F

742 Fliervoet, T.F., White, S.H., Drury, M.R., 1997. Evidence for dominant grain-boundary sliding
743 deformation in greenschist- and amphibolite-grade polymineralic ultramylonites from the
744 Redbank Deformed Zone, Central Australia. Journal of Structural Geology 19, 1495–
745 1520. https://doi.org/10.1016/S0191-8141(97)00076-X

746 Früh-Green, G.L., 1994. Interdependence of deformation, fluid infiltration and reaction
747 progress recorded in eclogitic metagranitoids (Sesia Zone, Western Alps). Journal of
748 Metamorphic Geology 12, 327–343. https://doi.org/10.1111/j.1525-1314.1994.tb00026.x

749 Gapais, D., 1989. Shear structures within deformed granites: mechanical and thermal
750 indicators. Geology 17, 1144–1147. https://doi.org/10.1130/0091-
751 7613(1989)017<1144:SSWDGM>2.3.CO

752 Gerbi, C., Johnson, S.E., Shulman, D., Klepeis, K., 2016. Influence of microscale weak zones
753 on bulk strength. Geochemistry, Geophysics, Geosystems 17, 4064–4077.
754 https://doi.org/10.1002/2016GC006551

755 Gerya, T. V., Stöckhert, B., Perchuk, A.L., 2002. Exhumation of high-pressure metamorphic
756 rocks in a subduction channel: A numerical simulation. Tectonics 21, 6-1-6–19.
757 https://doi.org/10.1029/2002TC001406

758 Getsinger, A.J., Hirth, G., 2014. Amphibole fabric formation during diffusion creep and the
759 rheology of shear zones. 535–538. https://doi.org/10.1130/G35327.1

760 Glodny, J., Austrheim, H., Molina, J.F., Rusin, A.I., Seward, D., 2003. Rb/Sr record of fluid-
761 rock interaction in eclogites: The Marun-Keu complex, Polar Urals, Russia. Geochimica
762 et Cosmochimica Acta 67, 4353–4371. https://doi.org/10.1016/S0016-7037(03)00370-3

763 Gueydan, F., Précigout, J., Montési, L.G.J., 2014. Strain weakening enables continental plate
764 tectonics. Tectonophysics 631, 189–196. https://doi.org/10.1016/J.TECTO.2014.02.005

765 Handy, M.R., 1994. Flow laws for rocks containing two non-linear viscous phases: A
766 phenomenological approach. Journal of Structural Geology 16, 287–301.
767 https://doi.org/10.1016/0191-8141(94)90035-3

768 Handy, M.R., 1990. The solid-state flow of polymineralic rocks. Journal of Geophysical
769 Research 95, 8647. https://doi.org/10.1029/JB095iB06p08647

770 Handy, M.R., 1989. Deformation regimes and the rheological evolution of fault zones in the
771 lithosphere: the effects of pressure, temperature, grainsize and time. Tectonophysics 163,
772 119–152. https://doi.org/10.1016/0040-1951(89)90122-4

773 Handy, M.R., Stünitz, H., 2002. Strain localization by fracturing and reaction weakening — a
774 mechanism for initiating exhumation of subcontinental mantle beneath rifted margins.
775 Geological Society, London, Special Publications 200, 387–407.
776 https://doi.org/10.1144/GSL.SP.2001.200.01.22

777 Hansen, L.N., Zimmerman, M.E., Dillman, A.M., Kohlstedt, D.L., 2012. Strain localization in
778 olivine aggregates at high temperature: A laboratory comparison of constant-strain-rate
779 and constant-stress boundary conditions. Earth and Planetary Science Letters 333–334,
780 134–145. https://doi.org/10.1016/J.EPSL.2012.04.016

781 Heilbronner, R., 2002. Analysis of bulk fabrics and microstructure variations using tesselations
782 of autocorrelation functions. Computers & Geosciences 28, 447–455.
783 https://doi.org/10.1016/S0098-3004(01)00088-7

784 Heilbronner, R.P., 1992. The autocorrelation function: an image processing tool for fabric
785 analysis. Tectonophysics 212, 351–370. https://doi.org/10.1016/0040-1951(92)90300-U

786 Herwegh, M., Linckens, J., Ebert, A., Berger, A., Brodhag, S.H., 2011. The role of second
787 phases for controlling microstructural evolution in polymineralic rocks: A review. Journal
788 of Structural Geology 33, 1728–1750. https://doi.org/10.1016/j.jsg.2011.08.011

789 Hidas, K., Tommasi, A., Garrido, C.J., Padrón-Navarta, J.A., Mainprice, D., Vauchez, A.,
790 Barou, F., Marchesi, C., 2016. Fluid-assisted strain localization in the shallow
791 subcontinental lithospheric mantle. Lithos 262, 636–650.
792 https://doi.org/10.1016/j.lithos.2016.07.038

793 Hirth, G., Tullis, J., 1992. Dislocation creep regimes in quartz aggregates. Journal of Structural
794 Geology 14, 145–159. https://doi.org/10.1016/0191-8141(92)90053-Y

795 Holyoke, C.W., Tullis, J., 2006a. Mechanisms of weak phase interconnection and the effects of
796 phase strength contrast on fabric development. Journal of Structural Geology 28, 621–640.
797 https://doi.org/10.1016/j.jsg.2006.01.008

798 Holyoke, C.W., Tullis, J., 2006b. Formation and maintenance of shear zones. Geology 34, 105–
799 108. https://doi.org/10.1130/G22116.1

800 Imon, R., Okudaira, T., Fujimoto, A., 2002. Dissolution and precipitation processes in deformed
801 amphibolites: an example from the ductile shear zone of the Ryoke metamorphic belt, SW
802 Japan. Journal of Metamorphic Geology 20, 297–308. https://doi.org/10.1046/j.1525-
803 1314.2002.00367.x

804 Jamtveit, B., Austrheim, H., Putnis, A., 2016. Disequilibrium metamorphism of stressed
805 lithosphere. Earth-Science Reviews 154, 1–13.
806 https://doi.org/10.1016/J.EARSCIREV.2015.12.002

807 Jordan, P., 1988. The rheology of polymineralic rocks - an approach. Geologische Rundschau
808 77, 285–294. https://doi.org/10.1007/BF01848690

809 Kanagawa, K., Shimano, H., Hiroi, Y., 2008. Mylonitic deformation of gabbro in the lower
810 crust: A case study from the Pankenushi gabbro in the Hidaka metamorphic belt of central
811 Hokkaido, Japan. Journal of Structural Geology 30, 1150–1166.
812 https://doi.org/10.1016/j.jsg.2008.05.007

813 Keller, L.M., Abart, R., Stünitz, H., De Capitani, C., 2004. Deformation, mass transfer and
814 mineral reactions in an eclogite facies shear zone in a polymetamorphic metapelite (Monte
815 Rosa nappe, western Alps). Journal of Metamorphic Geology 22, 97–118.
816 https://doi.org/10.1111/j.1525-1314.2004.00500.x

817 Kenkmann, T., Dresen, G., 2002. Dislocation microstructure and phase distribution in a lower
818 crustal shear zone - An example from the Ivrea-Zone, Italy. International Journal of Earth
819 Sciences 91, 445–458. https://doi.org/10.1007/s00531-001-0236-9

820 Kerrich, R., Allison, I., Barnett, R.L., Moss, S., Starkey, J., 1980. Microstructural and chemical
821 transformations accompanying deformation of granite in a shear zone at Mi??ville,
822 Switzerland; with implications for stress corrosion cracking and superplastic flow.
823 Contributions to Mineralogy and Petrology 73, 221–242.
824 https://doi.org/10.1007/BF00381442

825 Kilian, R., Heilbronner, R., Stünitz, H., 2011. Quartz grain size reduction in a granitoid rock
826 and the transition from dislocation to diffusion creep. Journal of Structural Geology 33,
827 1265–1284. https://doi.org/10.1016/j.jsg.2011.05.004

828 Kirby, S.H., Kronenberg, A.K., 1987. Rheology of the lithosphere: Selected topics. Reviews of
829 Geophysics 25, 1219. https://doi.org/10.1029/RG025i006p01219

830 Kohlstedt, D.L., Evans, B., Mackwell, S.J., 1995. Strength of the lithosphere: Constraints
831 imposed by laboratory experiments. Journal of Geophysical Research: Solid Earth 100,
832 17587–17602. https://doi.org/10.1029/95JB01460

833 Koons, P.O., Rubie, D.C., Fruch-Green, G., 1987. The Effects of Disequilibrium and
834 Deformation on the Mineralogical Evolution of Quartz Diorite During Metamorphism in
835 the Eclogite Facies. Journal of Petrology 28, 679–700.
836 https://doi.org/10.1093/petrology/28.4.679

837 Kruse, R., Stünitz, H., 1999. Deformation mechanisms and phase distribution in mafic high-
838 temperature mylonites from the Jotun Nappe, southern Norway. Tectonophysics 303, 223–
839 249. https://doi.org/10.1016/S0040-1951(98)00255-8

840 Langdon, T.G., 2006. Grain boundary sliding revisited: Developments in sliding over four
841 decades. Journal of Materials Science 41, 597–609. https://doi.org/10.1007/s10853-006-
842 6476-0

843 Linckens, J., Bruijn, R.H.C., Skemer, P., 2014. Dynamic recrystallization and phase mixing in
844 experimentally deformed peridotite. Earth and Planetary Science Letters 388, 134–142.
845 https://doi.org/10.1016/J.EPSL.2013.11.037

846 Linckens, J., Herwegh, M., Mntener, O., Mercolli, I., 2011. Evolution of a polymineralic mantle
847 shear zone and the role of second phases in the localization of deformation. Journal of
848 Geophysical Research: Solid Earth 116, 1–21. https://doi.org/10.1029/2010JB008119

849 Mansard, N., Raimbourg, H., Augier, R., Précigout, J., Le Breton, N., 2018. Large-scale strain
850 localization induced by phase nucleation in mid-crustal granitoids of the south Armorican
851 massif. Tectonophysics 745, 46–65. https://doi.org/10.1016/j.tecto.2018.07.022

852 Marti, S., Stünitz, H., Heilbronner, R., Plümper, O., Drury, M., 2017. Experimental
853 investigation of the brittle-viscous transition in mafic rocks – Interplay between fracturing,
854 reaction, and viscous deformation. Journal of Structural Geology 105, 62–79.
855 https://doi.org/10.1016/j.jsg.2017.10.011

856 Marti, S., Stünitz, H., Heilbronner, R., Plümper, O., Kilian, R., 2018. Syn-kinematic hydration
857 reactions , grain size reduction , and dissolution – precipitation creep in experimentally

858 deformed plagioclase – pyroxene mixtures. 985–1009. https://doi.org/10.5194/se-9-985-
859 2018

860 Menegon, L., Fusseis, F., Stünitz, H., Xiao, X., 2015. Creep cavitation bands control porosity
861 and fluid flow in lower crustal shear zones. Geology 43, 227–230.
862 https://doi.org/10.1130/G36307.1

863 Mitra, G., 1978. Ductile deformation zones and mylonites; the mechanical processes involved
864 in the deformation of crystalline basement rocks. American Journal of Science 278, 1057–
865 1084. https://doi.org/10.2475/ajs.278.8.1057

866 Montési, L.G.J., 2013. Fabric development as the key for forming ductile shear zones and
867 enabling plate tectonics. Journal of Structural Geology 50, 254–266.
868 https://doi.org/10.1016/j.jsg.2012.12.011

869 Montési, L.G.J., 2007. A constitutive model for layer development in shear zones near the
870 brittle-ductile transition. Geophysical Research Letters 34, 1–5.
871 https://doi.org/10.1029/2007GL029250

872 Newman, J., Lamb, W.M., Drury, M.R., Vissers, R.L.M., 1999. Deformation processes in a
873 peridotite shear zone: reaction-softening by an H2O-deficient, continuous net transfer
874 reaction. Tectonophysics 303, 193–222. https://doi.org/10.1016/S0040-1951(98)00259-5

875 Newman, J., Mitra, G., 1993. Lateral variations in mylonite zone thickness as influenced by
876 fluid-rock interactions, Linville falls fault, North Carolina. Journal of Structural Geology
877 15, 849–863. https://doi.org/10.1016/0191-8141(93)90180-I

878 Olgaard, D.L., 1990. The role of second phase in localizing deformation. Geological Society,
879 London, Special Publications 54, 175–181.
880 https://doi.org/10.1144/GSL.SP.1990.054.01.17

881 Palazzin, G., Raimbourg, H., Stünitz, H., Heilbronner, R., Neufeld, K., Précigout, J., 2018.
882 Evolution in H2O contents during deformation of polycrystalline quartz: An experimental
883 study. Journal of Structural Geology 114, 95–110.
884 https://doi.org/10.1016/J.JSG.2018.05.021

885 Panozzo, R., 1983. Two-dimensional analysis of shape-fabric using projections of digitized
886 lines in a plane. Tectonophysics 95, 279–294. https://doi.org/10.1016/0040-
887 1951(83)90073-2

888 Park, Y., Yoo, S.H., Ree, J.H., 2006. Weakening of deforming granitic rocks with layer
889 development at middle crust. Journal of Structural Geology 28, 919–928.
890 https://doi.org/10.1016/j.jsg.2006.02.005

891 Paterson, M.S., Luan, F.C., 1990. Quartzite rheology under geological conditions. Geological
892 Society, London, Special Publications 54, 299–307.
893 https://doi.org/10.1144/GSL.SP.1990.054.01.26

894 Paterson, M. S., 2013. Materials science for structural geology, Springer Dordrecht Heidelberg
895 New York London, p. 247, doi:10.1007/978-94-007-5545-1

896 Pec, M., Stünitz, H., Heilbronner, R., 2012. Semi-brittle deformation of granitoid gouges in
897 shear experiments at elevated pressures and temperatures. 38.
898 https://doi.org/10.1016/j.jsg.2011.09.001

899 Pec, M., Stünitz, H., Heilbronner, R., Drury, M., 2016. Semi-brittle flow of granitoid fault rocks
900 in experiments. Journal of Geophysical Research: Solid Earth 121, 1677–1705.
901 https://doi.org/10.1002/2015JB012513

902 Platt, J.P., 2015. Rheology of two-phase systems: A microphysical and observational approach.
903 Journal of Structural Geology 77, 213–227. https://doi.org/10.1016/j.jsg.2015.05.003

904 Poirier, J.P., 1980. Shear localization and shear instability in materials in the ductile field.
905 Journal of Structural Geology 2, 135–142. https://doi.org/10.1016/0191-8141(80)90043-7

906 Precigout, J., Gueydan, F., Gapais, D., Garrido, C.J., Essaifi, A., 2007. Strain localisation in the
907 subcontinental mantle — a ductile alternative to the brittle mantle. Tectonophysics 445,
908 318–336. https://doi.org/10.1016/J.TECTO.2007.09.002

909 Précigout, J., Stünitz, H., 2016. Evidence of phase nucleation during olivine diffusion creep: A
910 new perspective for mantle strain localisation. Earth and Planetary Science Letters 455,
911 94–105. https://doi.org/10.1016/j.epsl.2016.09.029

912 Précigout, J., Stünitz, H., Pinquier, Y., Champallier, R., Schubnel, A., 2018. High-pressure,
913 High-temperature Deformation Experiment Using the New Generation Griggs-type
914 Apparatus. Journal of Visualized Experiments : JoVE. https://doi.org/10.3791/56841

915 Précigout, J., Prigent, C., Palasse, L., Pochon, A., 2017. Water pumping in mantle shear zones.
916 Nature communications 8: 15736, https://doi.org/10.1038/ncomms15736

Prigent, C., Guillot, S., Agard, P., Lemarchand, D., Soret, M., Ulrich, M., 2018. Transfer of subduction fluids into the deforming mantle wedge during nascent subduction: Evidence from trace elements and boron isotopes (Semail ophiolite, Oman). Earth and Planetary Science Letters 484, 213–228. https://doi.org/10.1016/J.EPSL.2017.12.008

Raimbourg, H., Toyoshima, T., Harima, Y., Kimura, G., 2008. Grain-size reduction mechanisms and rheological consequences in high-temperature gabbro mylonites of Hidaka, Japan. Earth and Planetary Science Letters 267, 637–653. https://doi.org/10.1016/j.epsl.2007.12.012

Ramsay, J.G., 1980. Shear zone geometry: A review. Journal of Structural Geology 2, 83–99. https://doi.org/10.1016/0191-8141(80)90038-3

Ree, J.H., Kim, H.S., Han, R., Jung, H., 2005. Grain-size reduction of feldspars by fracturing and neocrystallization in a low-grade granitic mylonite and its rheological effect. Tectonophysics 407, 227–237. https://doi.org/10.1016/j.tecto.2005.07.010

Richter, B., Stünitz, H., Heilbronner, R., 2016. Stresses and pressures at the quartz-to-coesite phase transformation in shear deformation experiments. Journal of Geophysical Research: Solid Earth 121, 8015–8033. https://doi.org/10.1002/2016JB013084

Richter, B., Stünitz, H., & Heilbronner, R. (2018). The brittle-to-viscous transition in polycrystalline quartz: An experimental study. Journal of Structural Geology, 114, 1-21. https://doi.org/10.1016/j.jsg.2018.06.005

Rosenberg, C.L., Handy, M.R., 2005. Experimental deformation of partially melted granite revisited: implications for the continental crust. Journal of Metamorphic Geology 23, 19–28. https://doi.org/10.1111/j.1525-1314.2005.00555.x

Rudnick, R.L., Fountain, D.M., 1995. Nature and composition of the continental crust: A lower crustal perspective. Reviews of Geophysics 33, 267. https://doi.org/10.1029/95RG01302

Rutter, E.H., Brodie, K.H., 1988a. The role of tectonic grain size reduction in the rheological stratification of the lithosphere. Geologische Rundschau 77, 295–307. https://doi.org/10.1007/BF01848691

Rutter, E.H., Brodie, K.H., 1988b. The role of tectonic grain size reduction in the rheological stratification of the lithosphere. Geologische Rundschau 77, 295–307. https://doi.org/10.1007/BF01848691

947 Rybacki, E., Dresen, G., 2000. Dislocation and diffusion creep of synthetic anorthite
948 aggregates. Journal of Geophysical Research: Solid Earth 105, 26017–26036.
949 https://doi.org/10.1029/2000JB900223

950 Schmid, S.M., Paterson, M.S., Boland, J.N., 1980. High temperature flow and dynamic
951 recrystallization in carrara marble. Tectonophysics 65, 245–280.
952 https://doi.org/10.1016/0040-1951(80)90077-3

953 Schmid, S.M., 1982. Microfabric studies as Indicators of Deformation Mechanisms and Flow
954 Laws Operative in Mountain Building. In: Hsü, K.J. (Ed.), Mountain Building Processes.
955 Academic Press, pp. 95e110.

956 Stünitz, H., Fitz Gerald, J.D., 1993. Deformation of granitoids at low metamorphic grades: II.
957 Granular flow in albite rich mylonites. Tectonophysics 221, 299–324.
958 https://doi.org/10.1016/0040-1951(93)90164-F

959 Stünitz, H., Tullis, J., 2001. Weakening and strain localization produced by syn-deformational
960 reaction of plagioclase. International Journal of Earth Sciences 90, 136–148.
961 https://doi.org/10.1007/s005310000148

962 Tackley, P.J., 1998. Self-consistent generation of tectonic plates in three-dimensional mantle
963 convection. Earth and Planetary Science Letters 157, 9–22. https://doi.org/10.1016/S0012-
964 821X(98)00029-6

965 Tarantola, A., Diamond, L., Stünitz, H., 2010. Modification of fluid inclusions in quartz
966 by deviatoric stress I: experimentally induced changes in inclusion shapes and
967 microstructures. Contributions to Mineralogy and Petrology 160 (6), 825–843.
968 doi:10.1007/s00410-010-0509-z.

969 Tokle, L., Hirth, G., Behr, W.M., 2019. Flow laws and fabric transitions in wet quartzite. Earth
970 and Planetary Science Letters 505, 152–161. https://doi.org/10.1016/J.EPSL.2018.10.017

971 Tullis, J., Yund, R.A., 1985. Dynamic recrystallisation of feldspar: a mechanism for ductile
972 shear zone formation. Geology 13, 238–241. https://doi.org/10.1130/0091-
973 7613(1985)13<238:DROFAM>2.0.CO;2

974 Viegas, G., Menegon, L., Archanjo, C., 2016. Brittle grain-size reduction of feldspar, phase
975 mixing and strain localization in granitoids at mid-crustal conditions (Pernambuco shear
976 zone, NE Brazil). Solid Earth 7, 375–396. https://doi.org/10.5194/se-7-375-2016

977 Wassmann, S., Stöckhert, B., 2013. Rheology of the plate interface - dissolution precipitation
978 creep in high pressure metamorphic rocks. Tectonophysics 608, 1–29.
979 https://doi.org/10.1016/j.tecto.2013.09.030

980 Weaver, B.L., Tarney, J., 1984. Major and trace element composition of the continental
981 lithosphere. Physics and Chemistry of the Earth 15, 39–68. https://doi.org/10.1016/0079-
982 1946(84)90004-1

983 White, S.H., Burrows, S.E., Carreras, J., Shaw, N.D., Humphreys, F.J., 1980. On mylonites in
984 ductile shear zones. Journal of Structural Geology 2, 175–187.
985 https://doi.org/10.1016/0191-8141(80)90048-6

986 Whitmeyer, S.J., Wintsch, R.P., 2005. Reaction localization and softening of texturally
987 hardened mylonites in a reactivated fault zone, central Argentina. Journal of Metamorphic
988 Geology 23, 411–424. https://doi.org/10.1111/j.1525-1314.2005.00588.x

989 Wintsch, R.P., Christoffersen, R., Kronenberg, A.K., 1995. Fluid-rock reaction weakening of
990 fault zones. Journal of Geophysical Research: Solid Earth 100, 13021–13032.
991 https://doi.org/10.1029/94JB02622

992 Yonkee, W.A., Parry, W.T., Bruhn, R.L., 2003. Relations between progressive deformation and
993 fluid-rock interaction during shear-zone growth in a basement-cored thrust sheet, Sevier
994 orogenic belt, Utah. American Journal of Science 303, 1–59.
995 https://doi.org/10.2475/ajs.303.1.1

996 Yund, R.A., Tullis, J., 1991. Compositional changes of minerals associated with dynamic
997 recrystallizatin. Contributions to Mineralogy and Petrology 108, 346–355.
998 https://doi.org/10.1007/BF00285942

999

1000

1001

1002

1003

1004

1005

Figure Captions

Fig. 1. Sample assembly of the shear deformation experiments using a Griggs-type apparatus. (**a**) Schematic cross-section of the assembly. (**b**) Schematic drawing of sample geometry in a 3D view. Sample powder is inserted between 45° pre-cut alumina forcing blocks. Modified after Tarantola et al., 2010. (**c**) Sample geometry at the end of the experiment: th_0 = initial thickness, th_f = final thickness.

Fig. 2. Differential stress (MPa) versus shear strain (γ) curves. (**a**) Set of terms used to describe the mechanical data. (**b**) Stress-strain curves showing the mechanical behaviour of two pure plagioclase samples deformed at 800 and 900 °C. The mechanical curve of a pure pyroxene sample deformed at 900 °C with an initial coarser grain size (< 40 µm) is also plotted. (**c-d**) Set of experiments deforming an Opx + Plag mixture at different temperatures (800, 850 and 900°C), and at constant confining pressure, strain rate and water content. These experiments are separated in two graphs according to the different duration of the "run-in" section. The color coding refers to the temperature of the experiments.

Fig. 3. SEM-BSE images representative of microstructures documented in pure plagioclase (**a**) and pyroxene (**b-c**) experiments. (**a**) Plagioclase grain size refinement (blue arrows). (**b**) Extensive fracturing of pyroxene. (**c**) Close-up of the pyroxene grains showing extensive grain size refinement (orange arrows). pl = plagioclase.

Fig. 4. SEM-BSE transect of a part of high shear strain sample (**a**) and the related manually digitized phase map (**b**) showing the overall strain gradient in the shear zone from top to bottom. This transect is characterized by a heterogeneity in the amount of reaction and deformation. rp = reaction products, opx = orthopyroxene, cpx = clinopyroxene, pl = plagioclase, amph = amphibole, alumina FB = alumina forcing block.

Fig. 5. SEM-BSE images representative of microstructures observed in high shear strain experiments. (**a-b**) The reaction product appears as coronas around the original Opx_1 and as aggregates in low-strain zones. Pyroxene is locally fractured and filled with reaction product (white arrows). (**c-d**) The transition zone shows the development of fine-grained tails and shear bands extending at the edges of Opx_1. These tails form fine-grained mixed zones rich in Opx_2, Pl_2 and Amph. (**e-f**) High-strain zones textures are made of intercalated fine-grained polyphase shear bands. In these zones, there is an extensive phase mixing between Opx_2, Pl_2 and Amph. The original Pl_1 almost completely disappears, while some Opx_1 clasts, that are reduced in size, remains within these fine-grained mixed zones. opx = orthopyroxene, cpx = clinopyroxene, pl = plagioclase, amph = amphibole, qtz = quartz.

Fig. 6. SEM-BSE images representative of microstructures observed in high-strain zones. Three samples deformed to high-shear strain are documented: one deformed at 850°C (**a-b**) and two others deformed at 900°C (**c-d-e**). In each case, the high-strain zones are made of fine-grained polyphase shear bands, mainly composed of Opx_2, Pl_2 and Amph. However, the volume fraction of reaction product is larger at 850°C and the deformation is more localized compared to samples deformed at 900°C, which show more distributed deformation and lower amounts of amphiboles at shear zone scale. Opx = orthopyroxene, cpx = clinopyroxene, pl = plagioclase, amph = amphibole, qtz = quartz.

Fig. 7. Analysis of the transect of high shear strain sample (Fig. 4). (**a**) The amount of reaction product is higher in the high-strain zone compared to low-strain ones. (**b-c-d**) The ACF analysis reveal a higher aspect ratio in the high-strain zones, essentially related to the reaction product, which are preferentially oriented subparallel to the piston interfaces. For reference, panel (**a**) shows the evolution of phases volume fraction through the transect. To avoid errors, Opx_2 and Amph are grouped together. Panel (**b**) displays the bulk aspect ratio R*, while the panel (**c**) displays the individual aspect ratio R*. Panel (**d**) shows the preferred orientation α^* with respect to the piston interfaces. Opx = orthopyroxene, cpx = clinopyroxene, pl = plagioclase, amph = amphibole.

Fig. 8. Chemical composition of plagioclase (**a**), pyroxene (**b**), and amphibole (**c**). The chemical compositions of plagioclase and pyroxene are divided into three subsets: clast-core, clast-rim and fine grains.

Fig. 9. SEM-BSE images representative of microstructures observed in the hot-pressing experiments (**a-b**) and peak stress experiments (**c-d**). (**a-b**) Thin reaction coronas that start forming at the Opx_1-Pl_1 interphase boundaries. This consists essentially of Opx_2 and $Plag_2$. (**c**) Representative microstructures observed at peak stress where the reaction product starts to form aggregates that are partially connected in the direction of extension. (**d**) Irregular grain boundaries composed of small grains of newly formed reaction product. Opx = orthopyroxene, cpx = clinopyroxene, pl = plagioclase, amph = amphibole.

Fig. 10. SEM-BSE images showing characteristic microstructures of the nascent mixing of phases. (**a**) Incipient interconnection of thin fine-grained polyphase layers (yellow dotted outline) subparallel to the shear plane (horizontal direction). (**b**) Close-up of layers showing fine-grained mixture of Opx_2, Pl_2 and Amph. (**c**) Close-up of incipient mixing forming tails at the edges of original Opx_1. Opx = orthopyroxene, cpx = clinopyroxene, pl = plagioclase, amph = amphibole.

Fig. 11. Grain size evolution of pyroxene between peak stress experiment (mode: 15.6 µm) and the newly formed Opx_2 in fine-grained mixed zones in high shear strain experiments (mode: 0.2 µm). The black curve represents a best-fit to the log-normal distribution. The average value for the aspect ratio of new Opx grains is a/b = 1.23.

Fig. 12. Evolution of the amount of reaction product as a function of time in plagioclase – pyroxene experiments at 900°C. Symbols denote types of experiments performed, which include hot-pressing, peak stress, intermediate and high shear strain experiments. The graph (**a**) shows the different types of experiments, strain rate and associated mechanical data in stress-strain graph. (**b**) Evolution of the

volume fraction of reaction product (RP) with time, and effect of deformation on reaction and sample strength. Exponential curve fitting for hot-pressed or deformed samples are colour coded. One exponential curve for deformed samples is fitted for peak stress samples, while the other is fitted for higher shear strain samples. The duration of the deformed experiments is taken from the hit-point.

Fig. 13. Deformation mechanism map for wet pyroxene (**a**) and wet feldspar (**b**) at 900°C and 1 GPa as a function of differential stress and grain size. On this map, we plot the differential stress and grain size of Opx at peak stress and in mixed zones of high shear strain experiments in both cases, as we consider that the grain size of these phases is similar. The deformation conditions of the pure Plag sample is also plotted. The grain size is represented in box-and-whisker diagram. Individual boxes were limited by upper and lower quartiles, and within it the median (white lines) and the mode (blue lines) was defined. The flow laws for wet pyroxene are from Dimanov and Dresen (2005), while those for wet feldspar are from Rybacki and Dresen (2000). The grain size piezometer for Opx (yellow line) is taken from the study of Linckens et al. (2014).

Fig. 14. Schematic textural and microstructural evolution of plagioclase-pyroxene mixture from hot-pressing conditions (**1**) to strongly deformed shear zones (**3**), illustrating the different stages of strain localization and weakening during deformation.

Tables

Table. 1. Composition of plagioclase (Plag) and orthopyroxene (Opx) starting material.

Table. 2. Summary of experimental conditions. Type: HP - hot-pressing, PS: peak stress, D: deformed samples to varying amounts of shear strain. A cross marks is added to the type of deformation when the forcing blocks started to slip at the sample interface; τ_{peak}: differential stress at peak, τ_{flow}: steady-state differential stress, τ_{end}: differential stress at end of experiment, γ: shear strain, th_0: thickness initial of the shear zone, thf: final shear zone thickness.

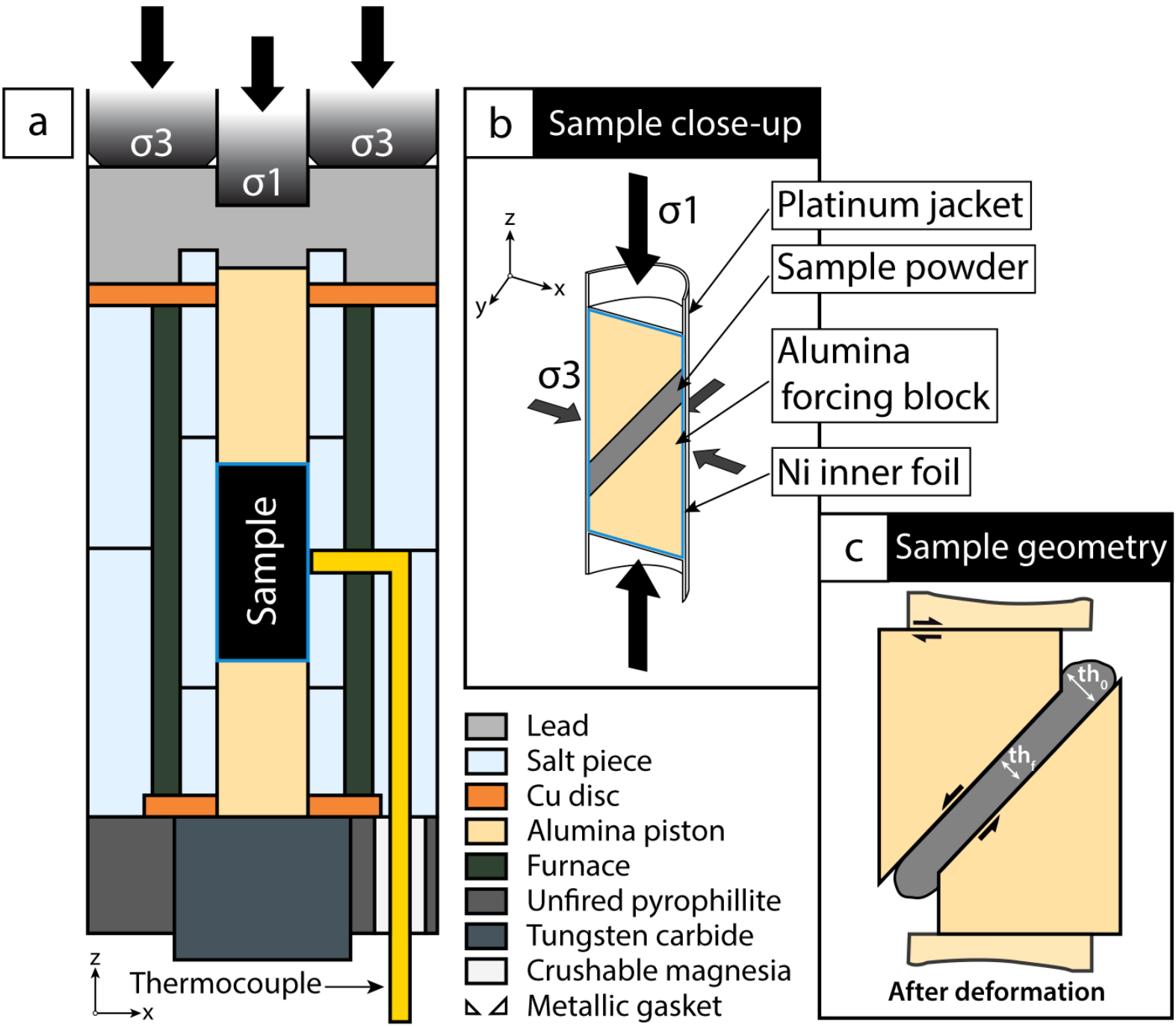
a
σ3
σ1
σ3
Sample
Thermocouple
z
x
b
Sample close-up
σ1
z
y
x
σ3
Platinum jacket
Sample powder
Alumina
forcing block
Ni inner foil
Lead
Salt piece
Cu disc
Alumina piston
Furnace
Unfired pyrophillite
Tungsten carbide
Crushable magnesia
Metallic gasket
c
Sample geometry
th0
thf
After deformation

Fig. 1.

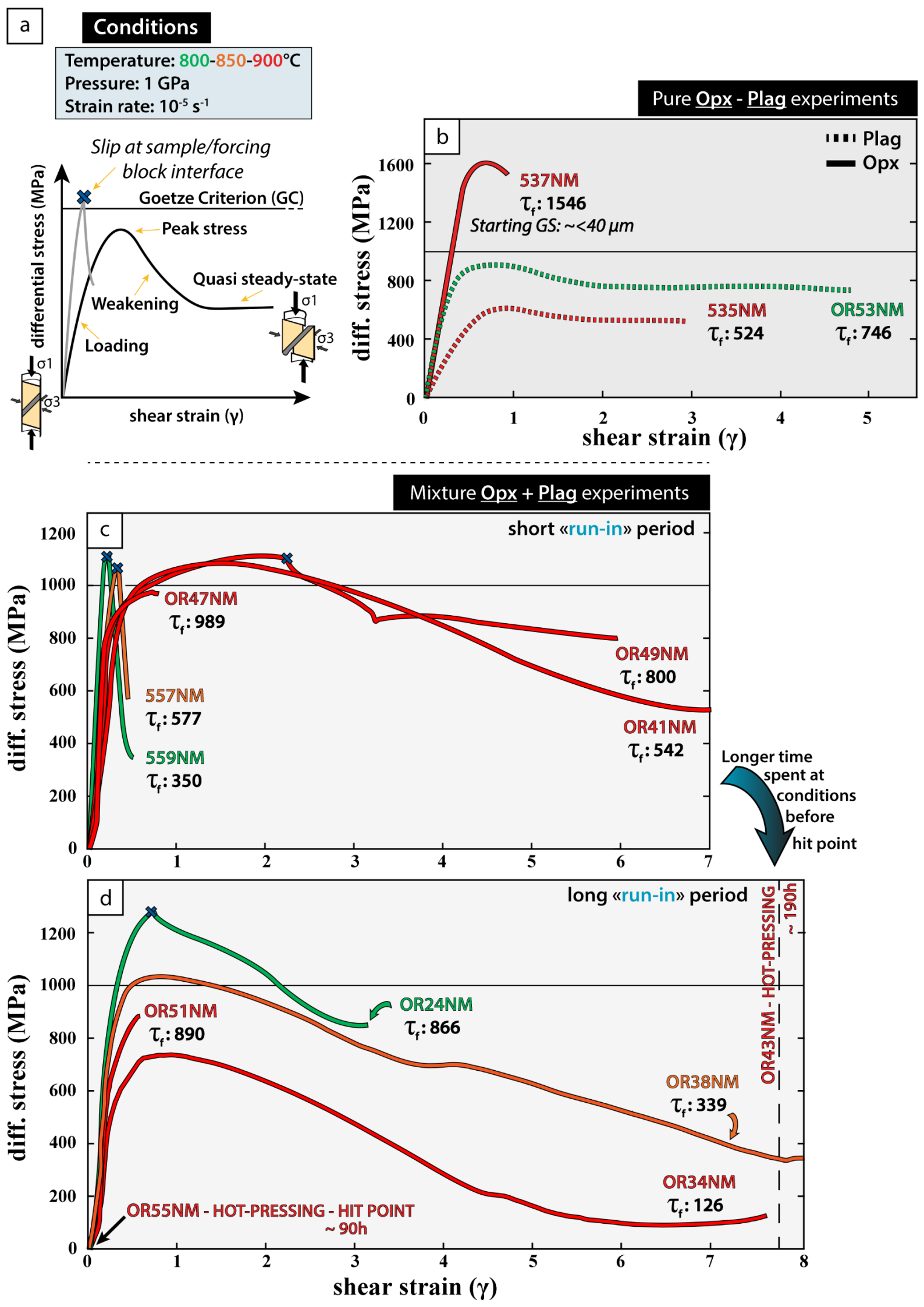
a
Conditions
Temperature: 800-850-900°C
Pressure: 1 GPa
Strain rate: 10-5 s-1
Slip at sample/forcing block interface
Goetze Criterion (GC)
Peak stress
Weakening
Quasi steady-state
Loading
σ1
σ3
differential stress (MPa)
shear strain (γ)
Pure Opx - Plag experiments
b
Plag
Opx
537NM
τf: 1546
Starting GS: ~<40 µm
535NM
τf: 524
OR53NM
τf: 746
diff. stress (MPa)
shear strain (γ)
Mixture Opx + Plag experiments
c
short «run-in» period
OR47NM
τf: 989
OR49NM
τf: 800
557NM
τf: 577
OR41NM
τf: 542
559NM
τf: 350
Longer time spent at conditions before hit point
d
long «run-in» period
OR43NM - HOT-PRESSING ~ 190h
OR51NM
τf: 890
OR24NM
τf: 866
OR38NM
τf: 339
OR34NM
τf: 126
OR55NM - HOT-PRESSING - HIT POINT ~ 90h
diff. stress (MPa)
shear strain (γ)

Fig. 2.

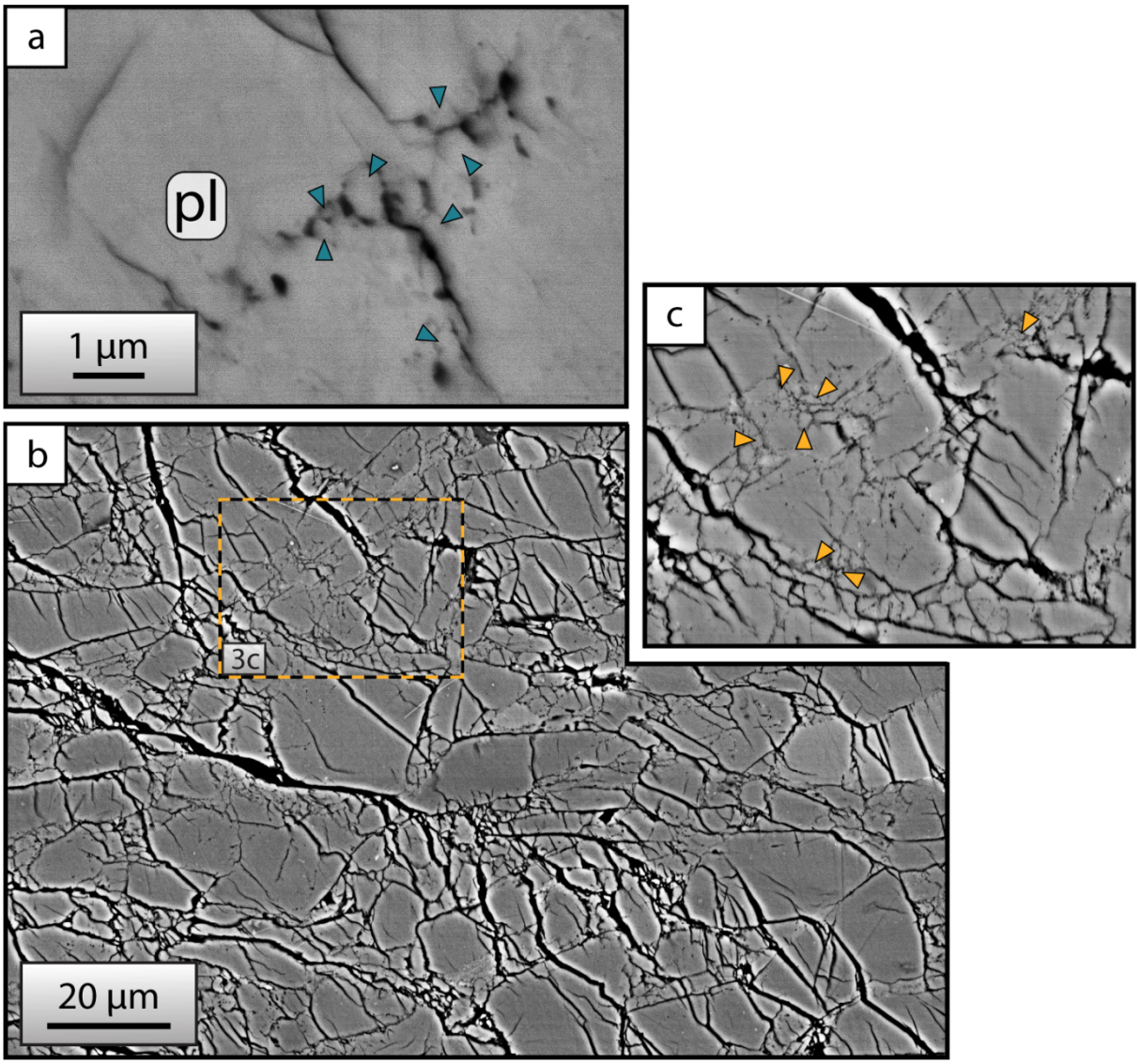

Fig. 3.

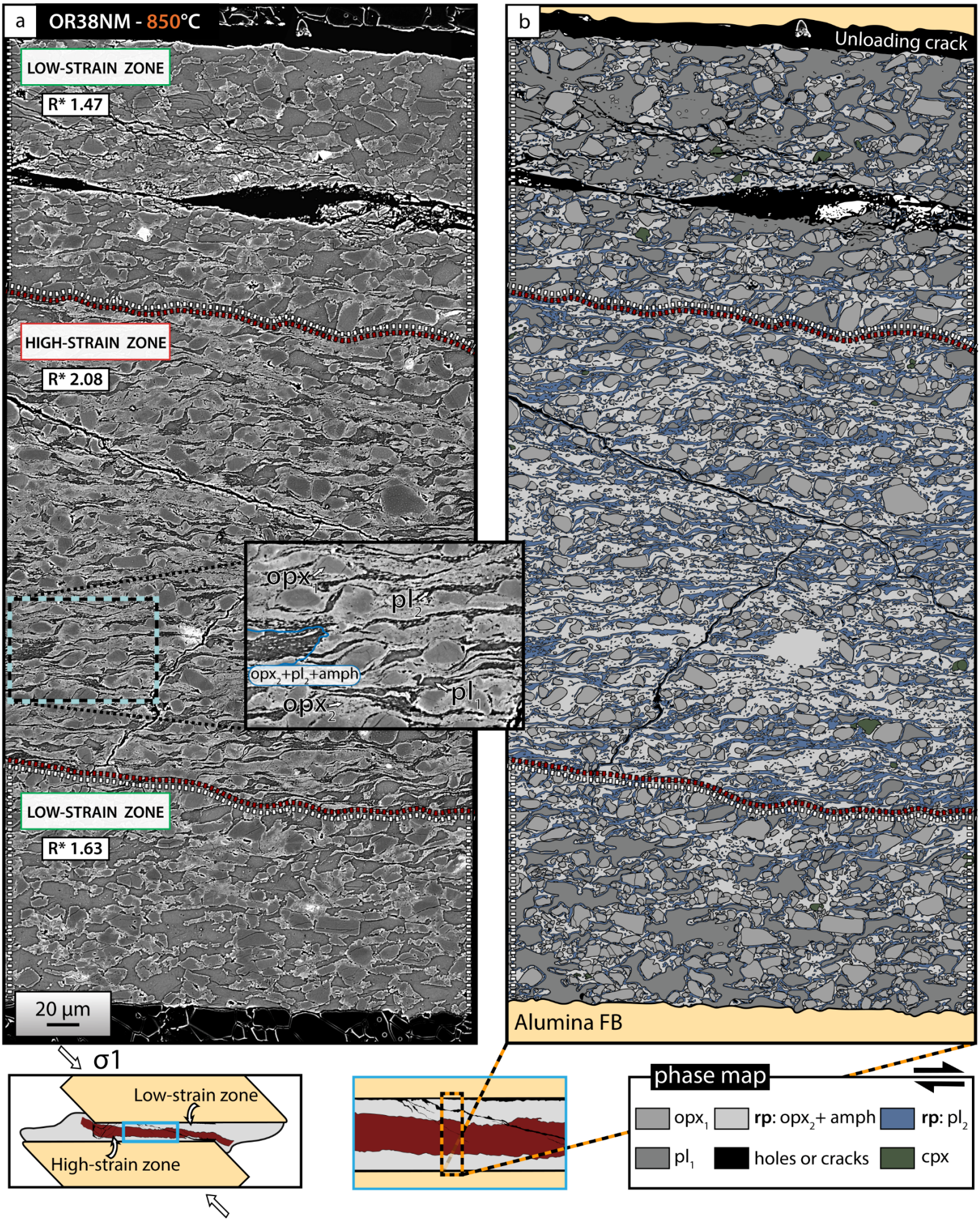
a
OR38NM - 850°C
LOW-STRAIN ZONE
R* 1.47
HIGH-STRAIN ZONE
R* 2.08
LOW-STRAIN ZONE
R* 1.63
20 µm
opx1
pl2
opx2+pl2+amph
opx2
pl1
b
Unloading crack
Alumina FB
σ1
Low-strain zone
High-strain zone
phase map
opx1
rp: opx2+ amph
rp: pl2
pl1
holes or cracks
cpx

Fig. 4.

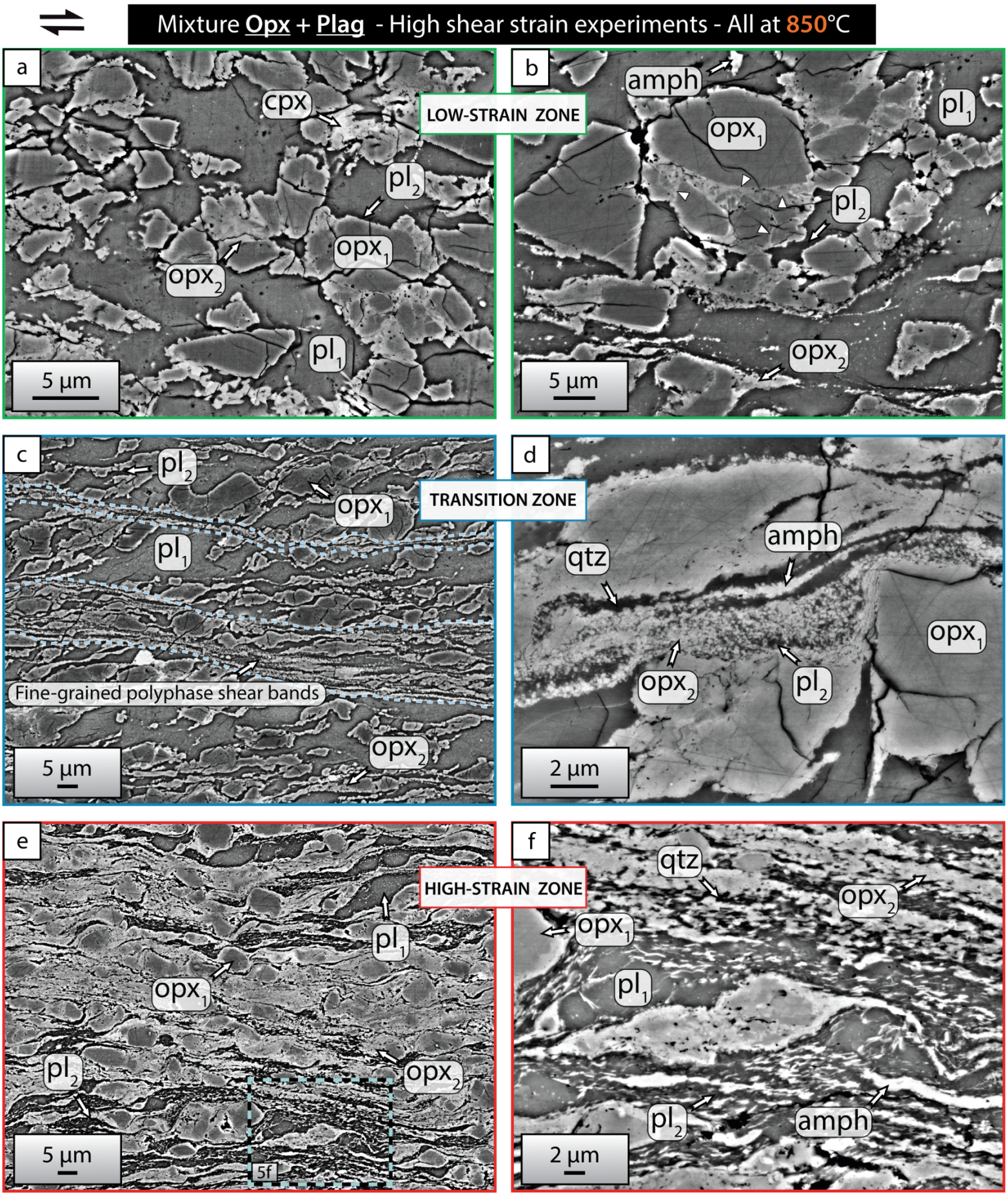
Mixture Opx + Plag - High shear strain experiments - All at 850°C
a
cpx
LOW-STRAIN ZONE
pl2
opx1
opx2
pl1
5 µm
b
amph
opx1
pl1
pl2
opx2
5 µm
c
pl2
opx1
TRANSITION ZONE
pl1
Fine-grained polyphase shear bands
opx2
5 µm
d
amph
qtz
opx1
opx2
pl2
2 µm
e
HIGH-STRAIN ZONE
pl1
opx1
pl2
opx2
5f
5 µm
f
qtz
opx2
opx1
pl1
pl2
amph
2 µm

Fig. 5.

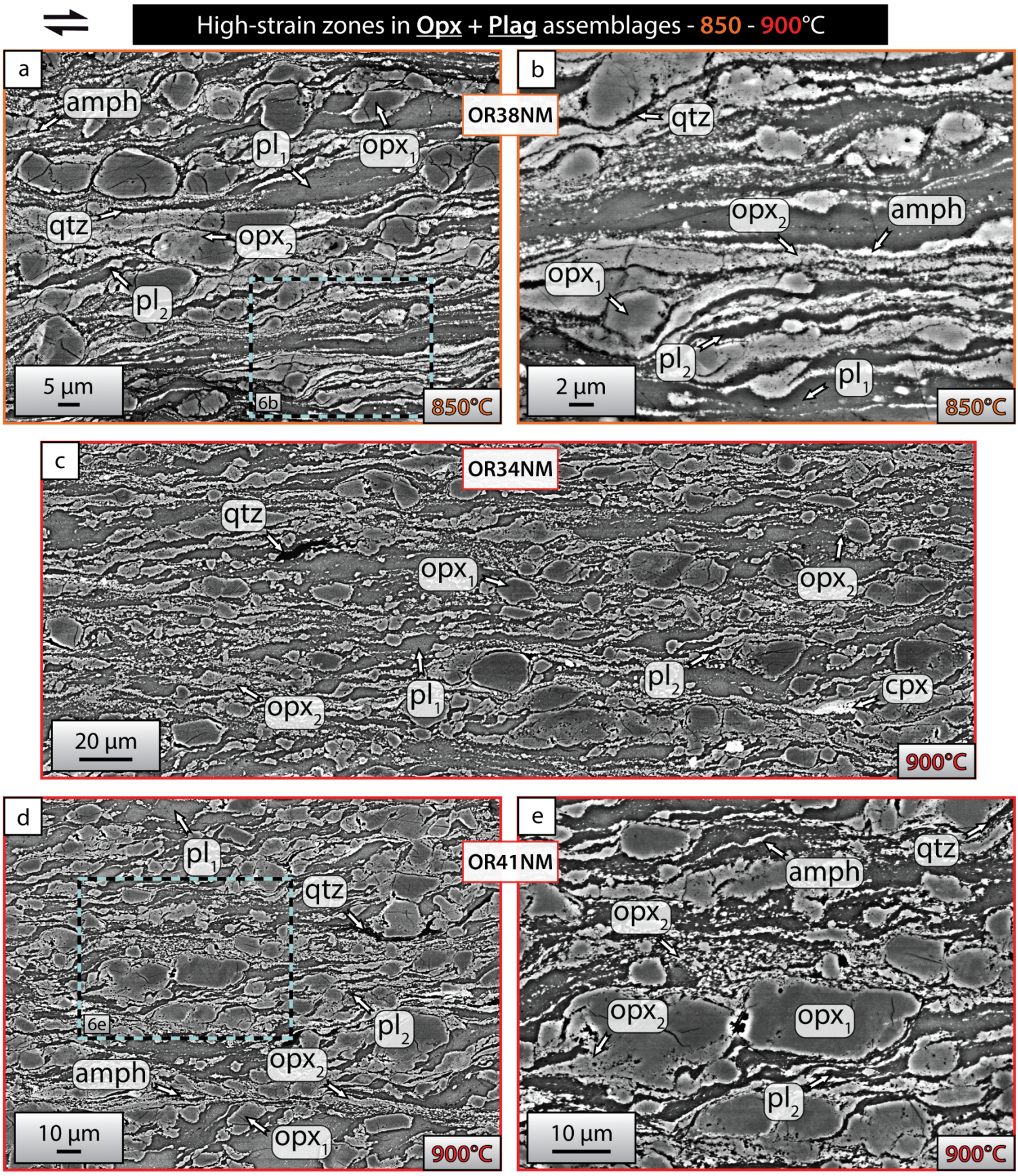
High-strain zones in Opx + Plag assemblages - 850 - 900°C
a
amph
pl1
opx1
qtz
opx2
pl2
6b
5 µm
850°C
OR38NM
b
qtz
opx2
amph
opx1
pl2
pl1
2 µm
850°C
c
OR34NM
qtz
opx1
opx2
pl1
pl2
cpx
opx2
20 µm
900°C
d
pl1
qtz
6e
pl2
opx2
amph
10 µm
opx1
900°C
e
OR41NM
qtz
amph
opx2
opx2
opx1
pl2
10 µm
900°C

Fig. 6.

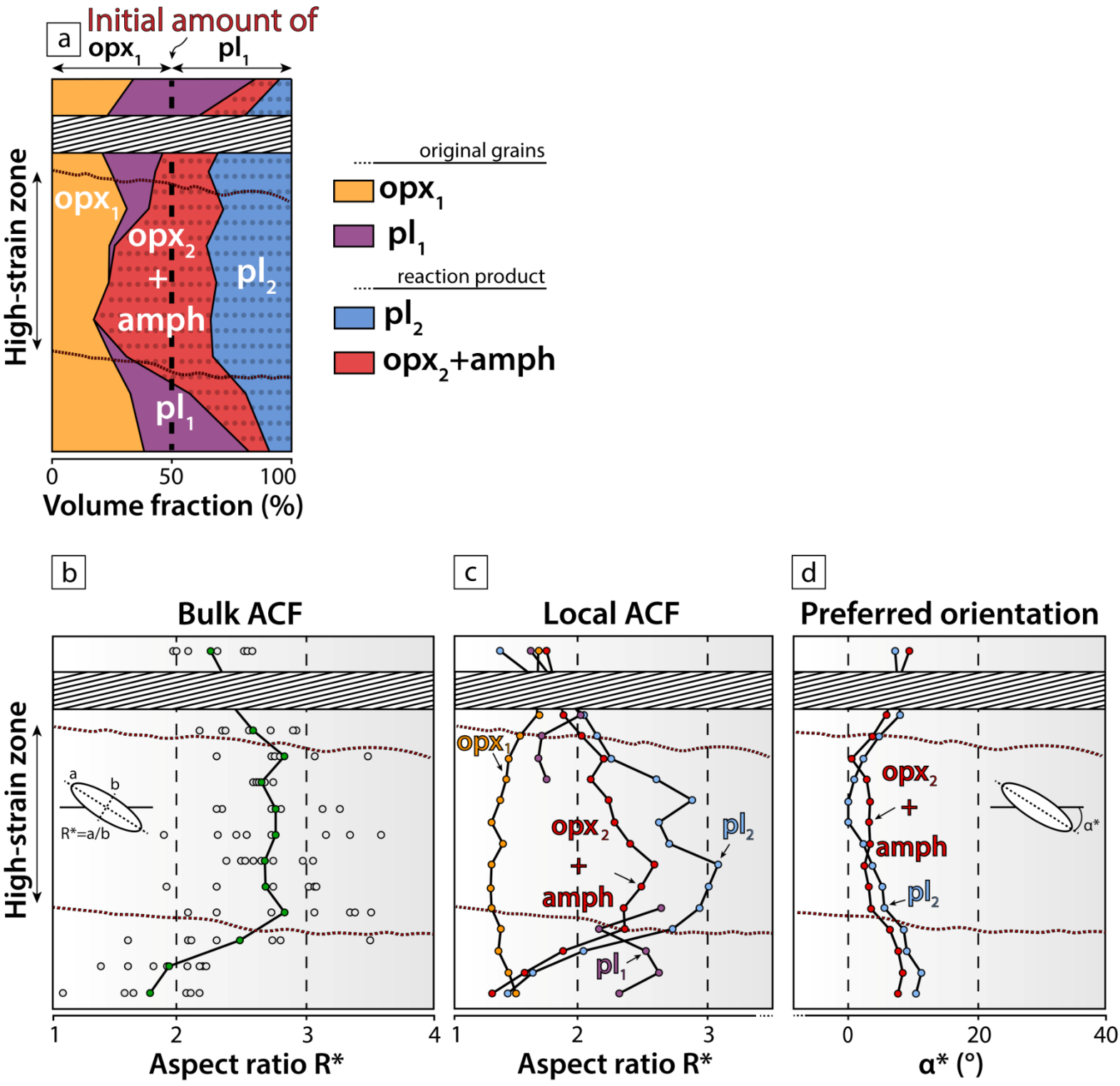
a
Initial amount of
opx1
pl1
High-strain zone
opx1
opx2
+
amph
pl2
pl1
0
50
100
Volume fraction (%)
original grains
opx1
pl1
reaction product
pl2
opx2+amph
b
Bulk ACF
c
Local ACF
d
Preferred orientation
High-strain zone
a
b
R*=a/b
opx1
opx2
+
amph
pl2
pl1
α*
1
2
3
4
Aspect ratio R*
0
20
40
α* (°)

Fig. 7.

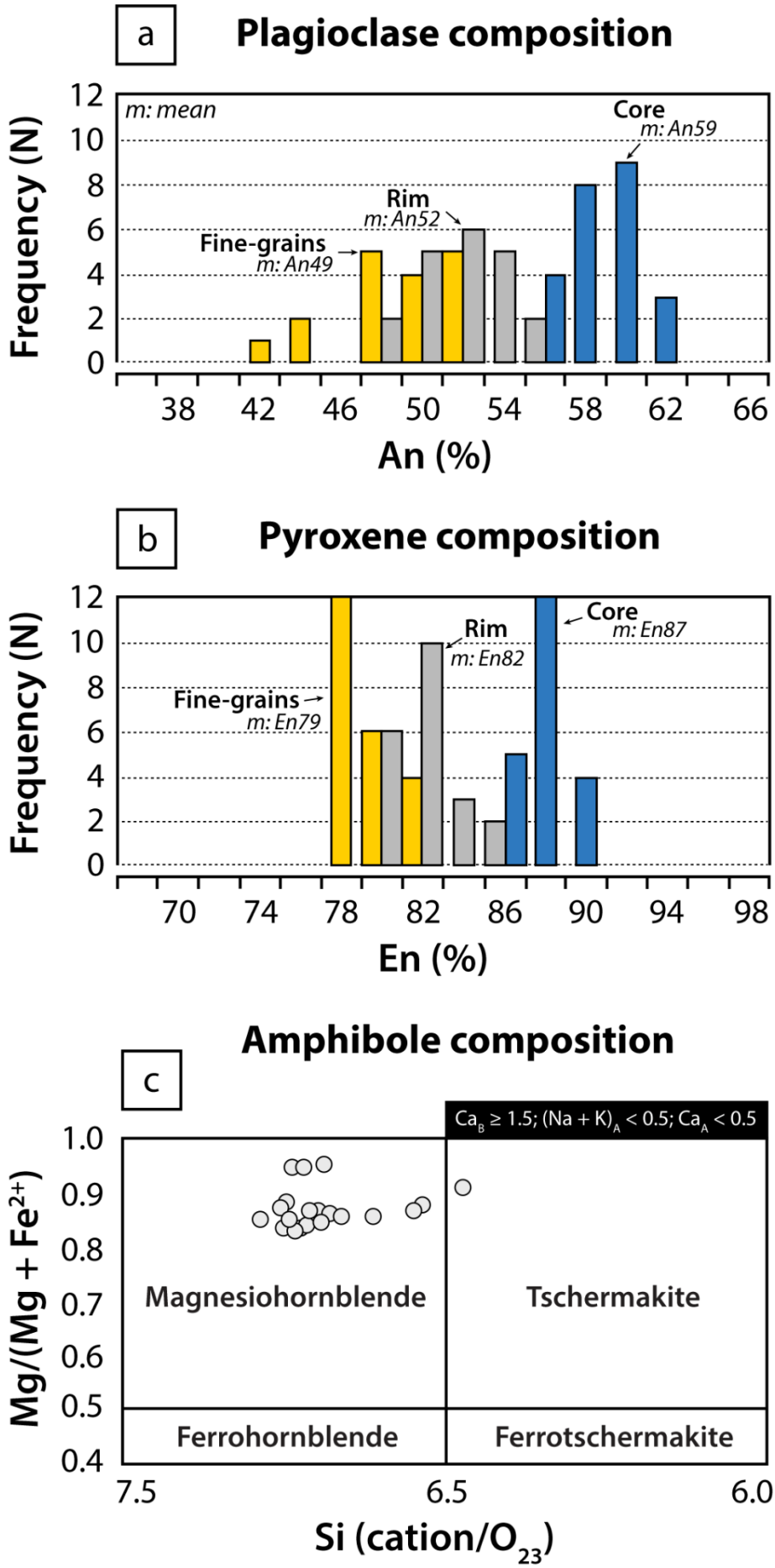
a
Plagioclase composition
m: mean
Core
m: An59
Rim
m: An52
Fine-grains
m: An49
Frequency (N)
An (%)
b
Pyroxene composition
Core
m: En87
Rim
m: En82
Fine-grains
m: En79
Frequency (N)
En (%)
Amphibole composition
c
Ca_B ≥ 1.5; (Na + K)_A < 0.5; Ca_A < 0.5
Magnesiohornblende
Tschermakite
Ferrohornblende
Ferrotschermakite
Mg/(Mg + Fe2+)
Si (cation/O23)

Fig. 8.

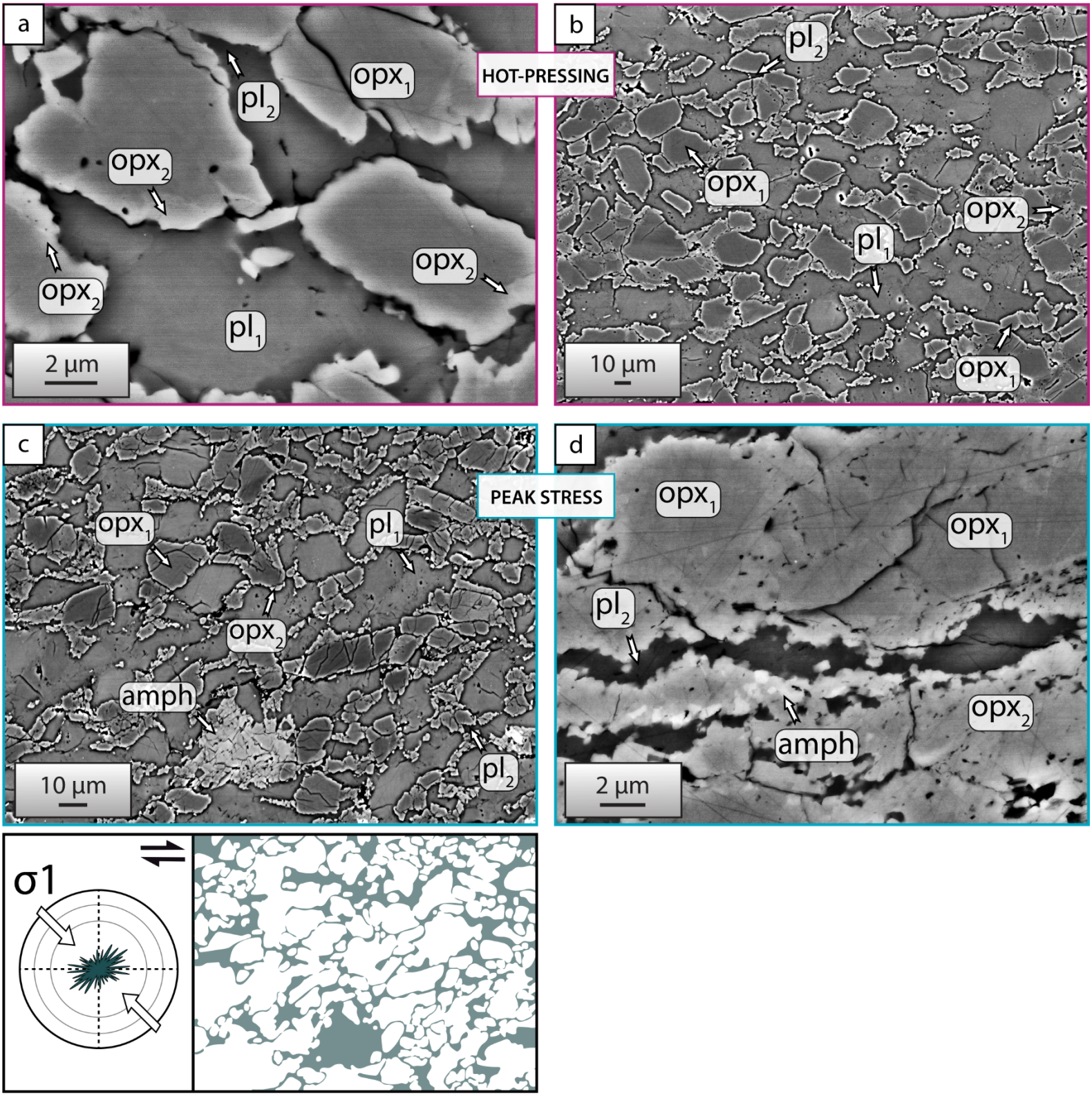
a
opx1
pl2
opx2
opx2
opx2
pl1
2 µm
HOT-PRESSING
b
pl2
opx1
opx2
pl1
opx1
10 µm
c
opx1
pl1
opx2
amph
pl2
10 µm
PEAK STRESS
d
opx1
opx1
pl2
opx2
amph
2 µm
σ1

Fig. 9.

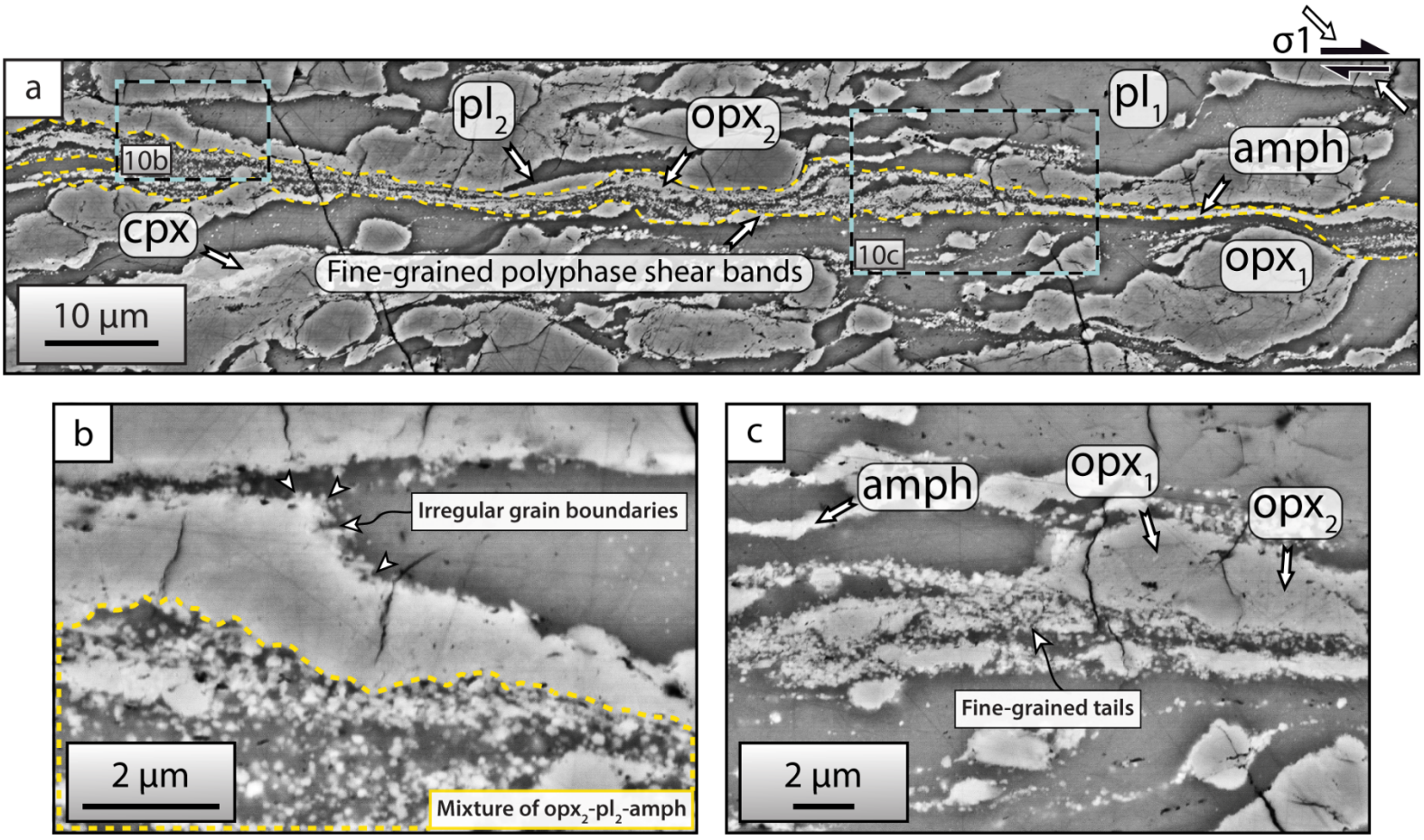
a
σ1
10b
pl2
opx2
pl1
amph
cpx
Fine-grained polyphase shear bands
10c
opx1
10 µm
b
Irregular grain boundaries
2 µm
Mixture of opx2-pl2-amph
c
amph
opx1
opx2
Fine-grained tails
2 µm

Fig. 10.

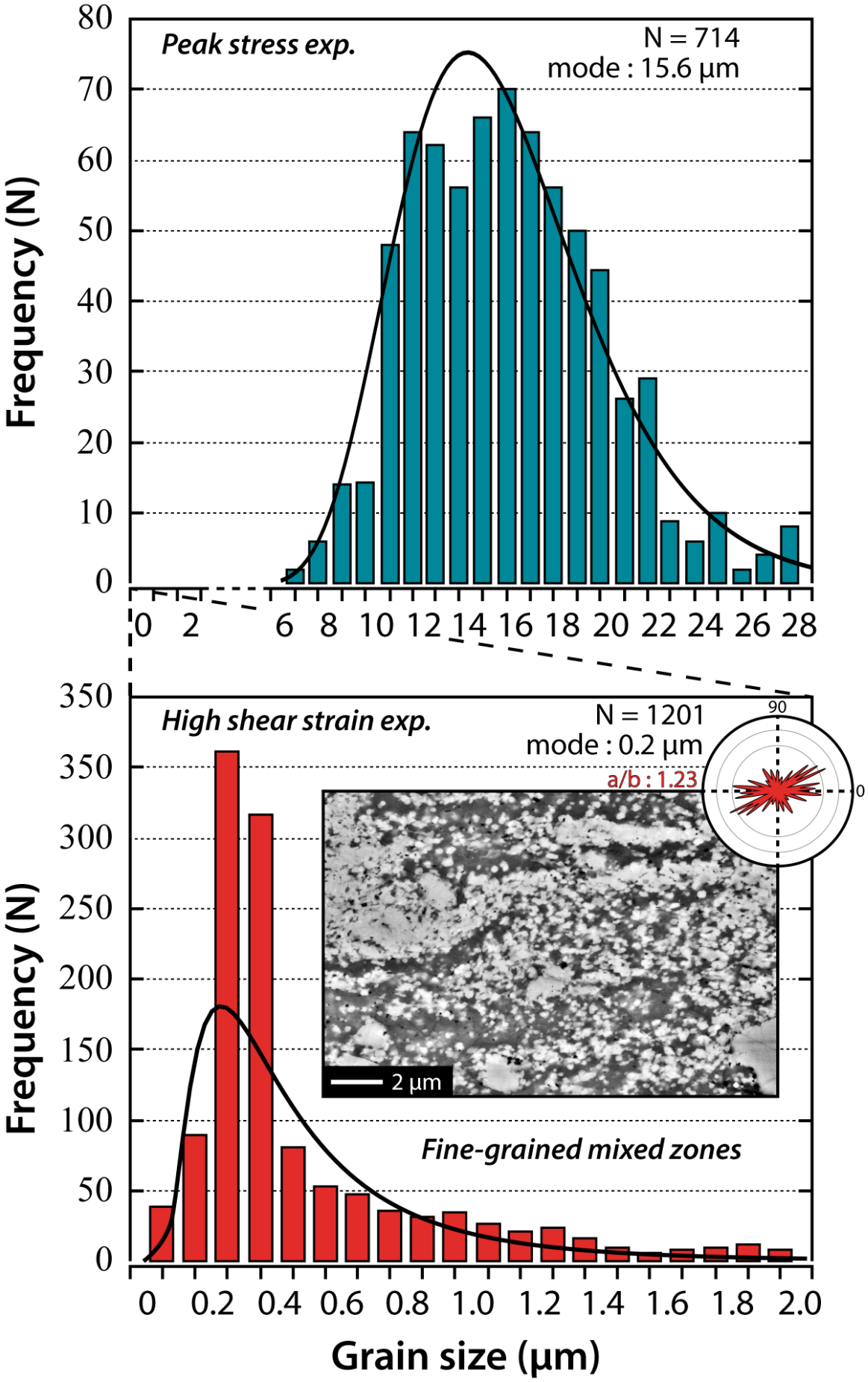
Peak stress exp.
N = 714
mode : 15.6 µm
Frequency (N)
High shear strain exp.
N = 1201
mode : 0.2 µm
a/b : 1.23
90
0
2 µm
Fine-grained mixed zones
Grain size (µm)

Fig. 11.

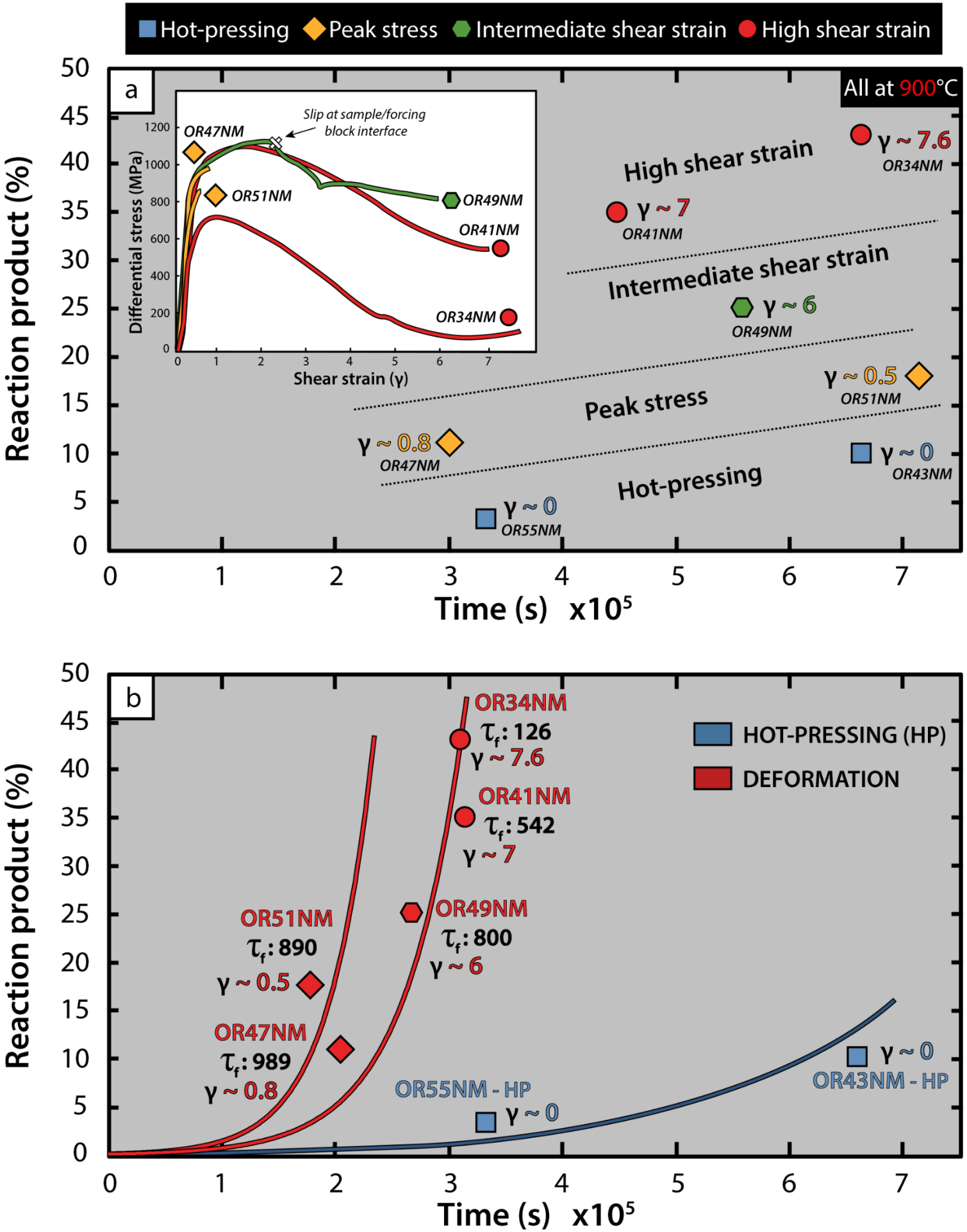
Hot-pressing
Peak stress
Intermediate shear strain
High shear strain
a
All at 900°C
Slip at sample/forcing block interface
OR47NM
OR51NM
OR49NM
OR41NM
OR34NM
Differential stress (MPa)
Shear strain (γ)
High shear strain
γ ~ 7.6
OR34NM
γ ~ 7
OR41NM
Intermediate shear strain
γ ~ 6
OR49NM
Peak stress
γ ~ 0.5
OR51NM
γ ~ 0.8
OR47NM
Hot-pressing
γ ~ 0
OR43NM
γ ~ 0
OR55NM
Reaction product (%)
Time (s) x10⁵
b
HOT-PRESSING (HP)
DEFORMATION
OR34NM
τf: 126
γ ~ 7.6
OR41NM
τf: 542
γ ~ 7
OR49NM
τf: 800
γ ~ 6
OR51NM
τf: 890
γ ~ 0.5
OR47NM
τf: 989
γ ~ 0.8
OR55NM - HP
γ ~ 0
γ ~ 0
OR43NM - HP
Reaction product (%)
Time (s) x10⁵

Fig. 12.

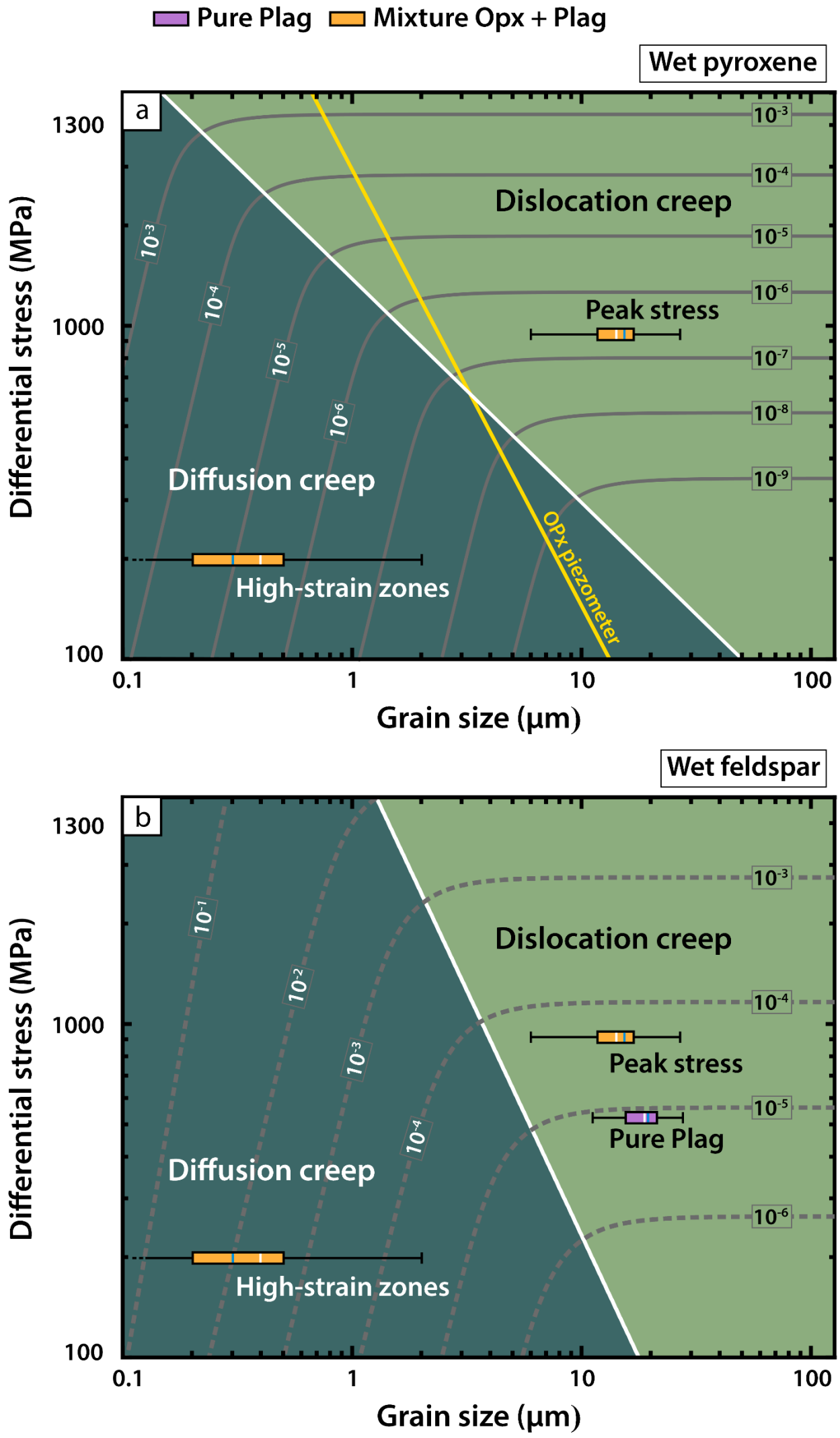
Pure Plag
Mixture Opx + Plag
Wet pyroxene
a
Dislocation creep
Diffusion creep
Peak stress
High-strain zones
OPx piezometer
10-3
10-4
10-5
10-6
10-7
10-8
10-9
Differential stress (MPa)
1300
1000
100
0.1
1
10
100
Grain size (µm)
Wet feldspar
b
Dislocation creep
Diffusion creep
Peak stress
Pure Plag
High-strain zones
10-1
10-2
10-3
10-4
10-5
10-6
Differential stress (MPa)
1300
1000
100
0.1
1
10
100
Grain size (µm)

Fig. 13.

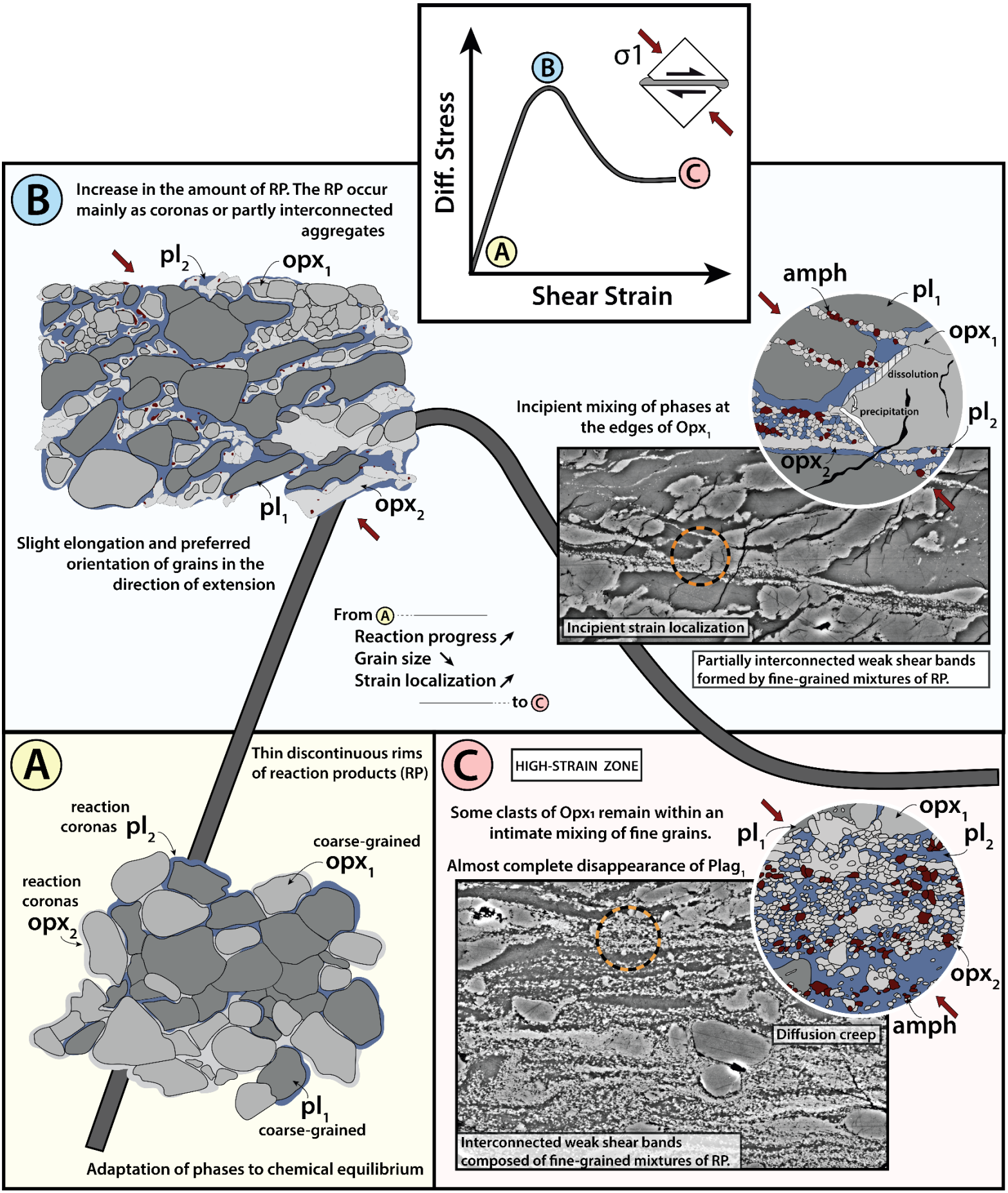
Diff. Stress
Shear Strain
σ1
B
C
A
B
Increase in the amount of RP. The RP occur mainly as coronas or partly interconnected aggregates
pl2
opx1
pl1
opx2
Slight elongation and preferred orientation of grains in the direction of extension
amph
pl1
opx1
dissolution
precipitation
pl2
opx2
Incipient mixing of phases at the edges of Opx1
Incipient strain localization
Partially interconnected weak shear bands formed by fine-grained mixtures of RP.
From A
Reaction progress ↗
Grain size ↘
Strain localization ↗
to C
A
Thin discontinuous rims of reaction products (RP)
reaction coronas pl2
coarse-grained opx1
reaction coronas opx2
pl1
coarse-grained
Adaptation of phases to chemical equilibrium
C
HIGH-STRAIN ZONE
Some clasts of Opx1 remain within an intimate mixing of fine grains.
Almost complete disappearance of Plag1
pl1
opx1
pl2
opx2
amph
Diffusion creep
Interconnected weak shear bands composed of fine-grained mixtures of RP.

Fig. 14.

Table. 1.

	***Sonoran* Plag**		***Damaping* Opx**	
	Wt. % oxides	Ions per 8 O	Wt. % oxides	Ions per 6 O
SiO_2	53,37	2,423	56,31	1,929
Al_2O_3	29,41	1,574	3,80	0,153
CaO	11,88	0,578	0,45	0,017
Na_2O	3,96	0,349	0,07	0,005
K_2O	0,46	0,027	0,02	0,001
MgO	0,09	0,006	33,42	1,707
TiO_2	0,08	0,03	0,07	0,002
FeO	0,38	0,014	6,31	0,181
MnO	0,05	0,002	0,18	0,005
Total	99,68	4,975	100,63	4,000
	An60		**Wo**1	
	Ab37		**En**89	
	Or3		**Fs**10	

Table. 2.

Exp. Nr	Material	Type	T	P	H_2O	τ_{peak}	τ_{flow}	τ_{end}	γ	th_0	th_f
			[°C]	[GPa]	µL	[MPa]	[MPa]	[MPa]		[mm]	[mm]
535NM	Plag	D	900	1	0,12	620	524	524	2,9	0,75	0,57
537NM	Opx	PS	900	1	0,12	1600	-	1546	0,9	0,75	0,69
557NM	Opx + Plag	PS^x	850	1	0,12	1067	-	577	0,4	0,75	0,59
559NM	Opx + Plag	PS^x	800	1	0,12	1111	-	350	0,5	0,75	0,67
OR24NM	Opx + Plag	D^x	800	1	0,25	1280	-	866	3,1	1,1	0,87
OR34NM	Opx + Plag	D	900	1	0,25	781	114	126	7,6	1,1	0,68
OR38NM	Opx + Plag	D	850	1	0,25	1038	339	339	8,0	1,1	0,63
OR41NM	Opx + Plag	D	900	1	0,25	1094	542	542	7,0	1,1	0,72
OR43NM	Opx + Plag	HP	900	1	0,25	-	-	-	-	1,1	1,1
OR47NM	Opx + Plag	PS	900	1	0,25	989	-	989	0,6	1,1	0,91
OR49NM	Opx + Plag	D^x	900	1	0,25	1111	800	800	6,0	1,1	0,73
OR51NM	Opx + Plag	PS	900	1	0,25	901	-	901	0,8	1,1	1
OR53NM	Plag	D	800	1	0,25	904	746	746	4,7	1,1	1
OR55NM	Opx + Plag	HP	900	1	0,25	-	-	-	-	1,1	1,1

Experimental data were processed using a MATLAB-based program inspired from the “rig” program of Dr. Matej Pec (Pec et al., 2016) and available at https://sites.google.com/site/jacquesprecigout/telechargements-downloads.